Materials Today Physics 50 (2025) 101632

Contents lists available at ScienceDirect

Materials Today Physics

journal homepage: www.journals.elsevier.com/materials-today-physics

Rapid prediction of phonon density of states by crystal attention graph neural network and high-throughput screening of candidate substrates for wide bandgap electronic cooling

Mohammed Al-Fahdi [a], Changpeng Lin [b], Chen Shen [c], Hongbin Zhang [c], Ming Hu [a,*]

[a] Department of Mechanical Engineering, University of South Carolina, Columbia, SC 29208, USA
[b] Theory and Simulation of Materials (THEOS), École Polytechnique Fédérale de Lausanne, CH-1015 Lausanne, Switzerland
[c] Institute of Materials Science, Technical University of Darmstadt, Darmstadt 64287, Germany

ARTICLE INFO

Keywords:
Graph neural network
Phonon density of states
Interfacial heat transfer
High-throughput screening
Wide bandgap electronics
Thermal management

ABSTRACT

Machine learning has demonstrated superior performance in predicting vast materials properties. However, predicting a spectral-like continuous material property such as phonon density of states (DOS) is more challenging for machine learning. In this work, with phonon DOS of 4994 inorganic structures with 62 unique elements calculated by density functional theory (DFT), we developed a crystal attention graph neural network (CATGNN) model for predicting total phonon DOS of crystalline materials. The computational cost of training the CATGNN model is several orders of magnitude cheaper than full DFT calculations. We find that high vibrational similarity or phonon DOS overlap is not the only requirement to obtain high interfacial thermal conductance (ITC) instead, the average acoustic group velocity of heat source and heat sink for the acoustic branches in the phonon DOS overlap region is equally important in determining ITC. Pearson correlation analysis yields a few simple material descriptors that are strongly but negatively correlated with ITC. These easy-to-calculate material features combined with the proposed high average acoustic group velocity and phonon DOS overlap predicted by CATGNN model offer a new reliable and fast route for high-throughput screening of novel crystalline materials with desirable high ITC for phonon-mediated thermal management of wide bandgap electronics.

1. Introduction

Machine learning has gained tremendous attention as a potent and robust approach to discover and explore functional materials in a broad materials space [1–7]. The success of machine learning is mainly due to its immense competence to correlating and predicting outputs provided with reasonable input features (called "descriptors") and sufficient high-quality data to detect hidden and uneasy-to-discover patterns from the provided data. Performing experiments to get high quality data of material properties can be extremely expensive in terms of cost, time, and resources. In contrast, high-throughput calculations via density functional theory (DFT) have largely been utilized to obtain a wide range of material properties with high precision and with no artificial input parameters to discover new materials with desirable properties [8–15]. Machine learning has been able to utilize atomic-level or compositional features along with structural features of various crystalline materials [16] and has demonstrated its excellence and massive success in predicting a wide variety of material properties with high accuracy comparable to DFT calculations including, but not limited to optical and electronic properties such as refractive index [17], bandgap [18], and superconductivity [19], mechanical properties such as bulk, shear, and Young's moduli, Poisson's ratio, and Vickers hardness [20–23], and thermal properties [24–26] such as heat capacity [27], thermal conductivity [28–30], and Debye temperature [31]. During the past decade, most material properties tackled in previous machine learning studies are discrete values and predicted based on the entire crystal structure, i.e., a specific crystalline topography corresponds to a single or several materials properties. For instance, a crystal structure would have a single value of bulk modulus and 3-component diagonal terms for thermal conductivity (in case of cubic structures, these 3 outputs can be even reduced to 1 due to the material symmetry). However, some other material properties that are remarkably and equally significant to study are continuous functions and have spectral-like formatting [32], e.g., the materials properties as a function

* Corresponding author.
E-mail address: hu@sc.edu (M. Hu).

https://doi.org/10.1016/j.mtphys.2024.101632
Received 3 October 2024; Received in revised form 15 December 2024; Accepted 18 December 2024
Available online 19 December 2024

of dependent variables such as dielectric function, absorption coefficient, electron density of states (DOS), and phonon DOS. Continuous and spectral-like properties pose several inherent challenges for machine learning related to the data itself, such as the high-demanding requirements of the data smoothing process and the special attention to peak positions which might trick machine learning models in determining the appropriate weights [33,34]. Moreover, spectral-like properties usually have different maximum values or cutoff among different materials, making the length and/or resolution of the data itself non-uniform across the training data and therefore it is hard to adapt the trained machine learning model to the new or unseen data.

In the recent years, graph neural networks (GNN) [35,36] have attracted a good deal of attention and are one of the fastest growing classes of machine learning models, due to their flexibility in modeling complex data structures in various fields such as social sciences [37], drug discovery [38], gene DNA [38], brain structures [39], and materials science [40]. GNN are constructed to represent graph-like data structures and to establish machine learning models based on the constituent nodes with the node features and the connecting edges and links [41]. GNN have already captivated the attention of researchers in the materials science community due to their capability in interpreting crystal structures constituted by atoms and bonds as graphs composed of nodes and edges, respectively [41]. GNN models operate on graph-structured data and have strong ties to the field of geometric deep learning, and thus are of particular relevance for materials chemistry and physics. The rapid development of GNNs has been demonstrated in a wide range of applications in chemistry and materials science and in the growing number of GNN-based packages such as Crystal Graph Convolutional Neural Networks (CGCNN) [42], Atomistic Line Graph Neural Networks (ALIGNN) [40], Global Attention Graph Neural Network (GATGNN) [43], and MatDeepLearn [44]. There are advantages and the potential to outperform other machine learning methods by GNN models and thus boost virtual materials design and materials science in general. This strongly motivates us to deploy GNN models to our specific material physics problem herein – interfacial thermal transport.

Large heat generation and insufficient heat removal mechanisms due to inherent limitations in manufacturing methods and materials employed in electronics have become the bottleneck that hinders the disruptive development of high-power electronic device technologies such as high electron mobility transistors (HEMTs) with wide bandgap materials [45,46]. From a scientific point of view, high interfacial thermal conductance (ITC) across the solid-solid interface is crucial for solving the critical issue of thermal management of high heat flux electronic devices. However, direct high-throughput DFT calculations of ITC for large amount of possible material pairs forming the interfaces are too computationally expensive and not practical. Previous interfacial thermal transport theory indicates that ITC is directly linked to the phonon DOS at the interface, which inspires us to use machine learning to train and predict phonon DOS and then "transfer" the information or knowledge to screen candidate substrate materials for potentially high ITC. In this work, we implement a crystal attention graph neural network (CATGNN) model to predict total phonon DOS using only atomic positions and species as inputs. The total phonon DOS predictions are then used to screen possible combinations of candidate materials through direct contact. We elucidate the hidden relationship and strong correlation between high ITC and high average acoustic group velocity of both heat sources and heat sinks, along with the previously known descriptor of high phonon DOS overlap. We also conducted Pearson correlation analysis on ITC and identified a few simple material descriptors that are strongly but negatively correlated with ITC. These easy-to-calculate material features combined with the aforementioned criteria of high average acoustic group velocity and phonon DOS overlap offer a new and reliable route for designing and fast screening large-scale material pairs with high ITC at the interfaces for thermal management of wide bandgap HEMT electronics.

2. First principle computational calculations

All the 4994 crystal structures used for training our CATGNN model are obtained from the Open Quantum Materials Database (OQMD) [8] which include binary, ternary, and quaternary compounds. There are 1161 noncubic and 3333 cubic structures in the training, validation, and testing dataset. The data distribution of space groups and number of atoms for the primitive cells of all structures is shown in Fig. S1 in Supplemental Information. All 4994 data including OQMD ID, formula and phonon DOS values are provided in the supplementary dataset. First, these structures are re-optimized by performing first principles calculations with the converged computational parameters to reach the ground state using Vienna Ab Initio Simulation package (VASP) [47–49]. The convergence criteria for crystal structures optimization are 10^{-8} eV and 10^{-4} eV/Å for the total energy and atomic forces, respectively. The optimization calculations fully allow the cell shape, cell volume, and atomic positions to change to reach the global minimum of potential energy surface of each structure. The Pedrew-Burke-Ernzerhof (PBE) parametrization of the generalized-gradient-approximation (GGA) is applied to describe the exchange-correlation effects of electrons [50] within the projector augmented wave (PAW) pseudopotentials [51]. The plane wave kinetic energy cutoff of 520 eV in the basis set of the electronic charge density wavefunction is set for all materials. The Brillouin zone was sampled using the Monkhorst-Pack k-mesh depending on the lattice constants, with the density of k-points sampling of 0.2 $Å^{-1}$ [52] to guarantee high quality of DFT calculations. It should be noted that our purpose of re-optimization is not to find global minima of the structures. Instead, we just want to get more accurate lattice parameters and atomic positions so that their phonon transport properties will be more accurate. That being said, our re-optimization does not guarantee the new structures will reach global minima as compared with the original structures from OQMD. We emphasize that our stricter convergence criteria implemented during DFT calculations should have a higher chance to reach global minima for some materials phases. For each optimized structure, we then generated 12 to 30 supercells, with random displacement of 0.03 Å for each atom in the supercell and the atomic forces evaluated for these displaced supercells by VASP. The supercell size depends on the symmetry of the primitive cell of the structure and the total number of atoms in the supercells generally ranges between 80 and 240. The supercells are constructed such that the lattice vectors of the supercells in the three crystallographic directions are more or less the same. The convergence criterion for supercell SCF DFT runs is 10^{-6} eV for the energy. After that, we fitted the harmonic (2nd order) and anharmonic (3rd order) interatomic force constants (IFCs) by the compressive sensing lattice dynamics (CSLD) method [53–55] with the 3rd-order force constants truncated to the 3rd nearest neighbor. With the 2nd order IFCs obtained, the phonon dispersions and phonon DOS are then calculated using PHONOPY [56]. The quality of phonon dispersions and DOS of selected structures is also validated by comparing with those obtained from the finite displacement method and density functional perturbation theory (DFPT), and the validation results of 8 selected materials can be found in Figure S2 and Figure S3 in Supplemental Information for phonon dispersion and phonon DOS, respectively. Finally, using the 2nd and 3rd IFCs as inputs, the lattice thermal conductivity (LTC) of structures is calculated by iteratively solving phonon Boltzmann transport equation using the ShengBTE package [57]. The NGRIDS parameter in ShengBTE is set such that (1) the product of NGRIDS and corresponding lattice length for all directions is more or less; (2) the NGRIDS is large enough to ensure the total number of phonon scattering channels is at least 1×10^8. Such settings will yield converged LTC results using the anharmonic IFCs up to the 3rd order. The ITC for interfaces formed by two candidate materials in contact is calculated using the almaBTE package [58] which implements Monte Carlo simulations and uses diffusive mismatch model (DMM) to approximate the interfacial phonon transmission coefficient. Highly dense grids of $24 \times 24 \times 24$ and $15 \times 15 \times 15$ were implemented

in the calculations for cubic (such as cubic GaN denoted as "c-GaN") and noncubic (such as wurtzite or hexagonal GaN denoted as "h-GaN") structures, respectively.

3. Results and discussion

a) CATGNN model architecture, training, and prediction of total phonon DOS

The general outline of our CATGNN model training and prediction is shown in Fig. 1. The crystal structures are first converted into graphs within a certain cutoff after implementing periodic boundary conditions. R_{max} is the maximum cutoff radius up to which the neighbors of each atom in the structure are considered. It is worth noting that, determining the cutoff radius (R_{max}) is extremely crucial in training the CATGNN model because the model needs to have an adequate graph with sufficient information from the neighboring environment for each node (i.e., atom). Having a large cutoff radius increases the number of neighbors, but it also makes the graph bigger and consequently increases the computational cost. A smaller R_{max} makes the graph smaller and reduces the computational cost, but the graph may not capture enough data from the neighboring environment for each node. The cutoff radius or R_{max} is generally around 4 to 8 Å which has been widely implemented in various GNN algorithms and methodologies [40,42–44]. Such a cutoff radius is physically meaningful for most inorganic solid crystals from a general interatomic interaction distance point of view. After some testing, we select R_{max} of 4.5 Å in this work. This cutoff radius is also on the same order as previous DFT studies on phonon transport properties of various systems where 3rd nearest neighbor cutoff distance is usually used [59–64]. Previous DFT calculations and convergence test on phonon properties of inorganic crystals suggest that using larger cutoff distance will not significantly affect the phonon results. Moreover, to test the possible effect of different cutoff distances, we performed additional training with cutoff distance being increased to 10 Å. As can be seen from Fig. S4 in Supplemental Information, the validation loss may not be significantly different from the previous training results with a 4.5 Å cutoff radius. Training with a much larger cutoff distance simply increases the computational cost without loss improvement. This confirms that our original 4.5 Å cutoff distance is enough to capture the local environment for each atom. We used the CGCNN features as node features (f) [42]. We also use one-hot encoding atomic number feature vector as node attributes (f'). Encoding the atomic number gives the model information on the species' mass since the value "1" is at the atomic number index in the one-hot encoding atomic number feature vector. The mass of an element is a known quantity for governing the phonon DOS which makes it a good node feature for our model as pointed out by Slack's model [65]. It is also known that the phonon DOS for light elements tend to have higher frequencies whereas heavier elements tend to have lower frequency phonon modes [66]. Therefore, using one-hot encoding atomic number feature vector as a node attribute is helpful in encoding mass as well. The edge features (e_{ij}) and edge attributes (e'_{ij}) are spherical harmonics and gaussian expansion of the bond lengths, respectively. The CATGNN model with all its layers is constructed with Pytorch [67] operating backend. Pytorch Geometric [68] was also used to construct CATGNN especially in message passing, mean pooling, and loading the graph data such as node features, node attributes, etc. It is also worth mentioning that the convolution and gate layers are imported from the e3nn package [28,69,70] with minor modifications to properly account for structures periodicity. However, the following two types of layers: (1) multi-head augmented crystal attention and (2) atom attention layer are developed from scratch and explained in more details below. The convolution and gate layers can be explained through the following formula:

$$v'_i = \frac{1}{\sqrt{n}} \sum_j v_j \otimes \left(h\left(\left|\left|u_{ij}\right|\right|\right)\right) Y\left(\frac{u_{ij}}{\left|\left|u_{ij}\right|\right|}\right) \quad (1)$$

where j are neighbors for node i, v'_i and v_j are updated node feature outputs and neighboring node messages, respectively, n is the average of nodes degree, h is a multilayer perceptron, u_{ij} is the relative vector from j

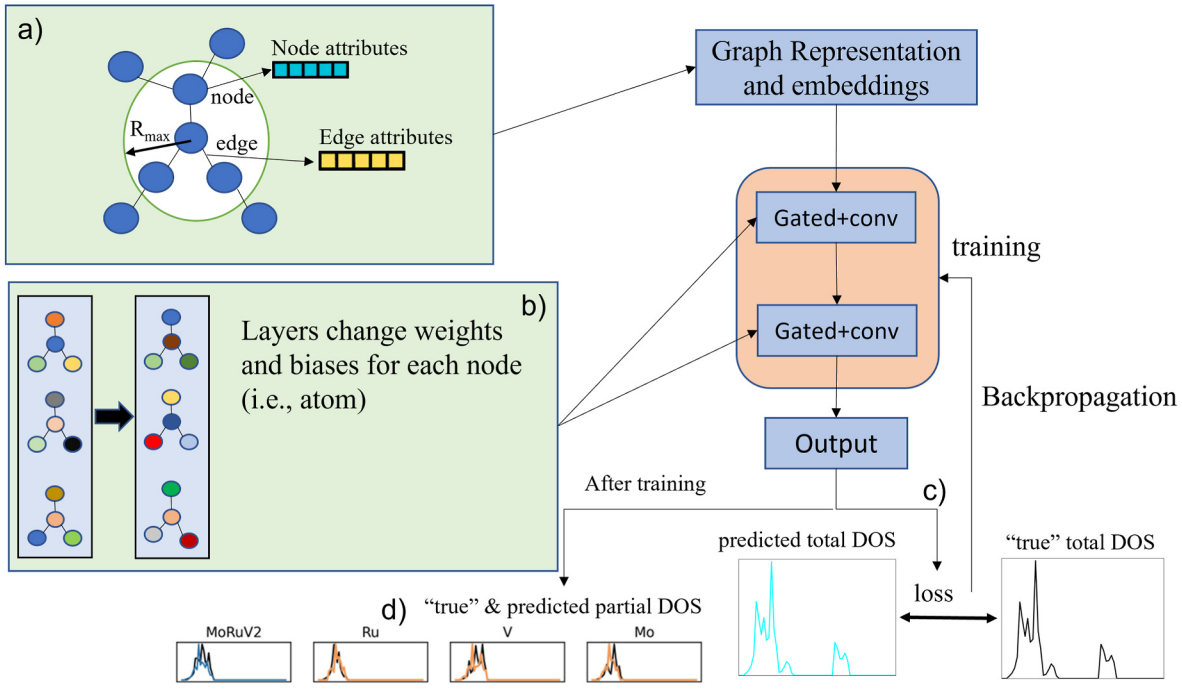

Fig. 1. Detailed framework of the Crystal Attention Graph Neural Network (CATGNN) model. Crystal structures represented as graphs within certain cutoffs with periodic boundary conditions with the node features (f) and node attributes (f') and edge features (e_{ij}) and edge attributes (e'_{ij}). Convolution, gated, multi-head augmented crystal attention, and single head atom attention layers simple explanations and brief formulas. Outputting the predicted total phonon DOS of crystal structure with forward and back propagation to minimize the loss in total DOS.

to i, and Y represents the spherical harmonics basis set. Relu activation function is used after the last convolution layer. Essentially, the weights and biases of the source nodes in each convolution layer previous layer inputs get updated based on the message from the neighboring nodes. The multi-head augmented crystal attention layers are defined by

$$v_i' = v_i + \sum_j \frac{\sum_h^{hs} softmax\left(g\left(BN\left(W_{att} \odot g\left(g(W_i \odot v_i^*) \oplus g\left(W_j \odot v_j^*\right)\right)\right)\right)\right) \odot v_j^*}{hs} = v_i + \sum_j \alpha \odot v_j^*$$
$$\alpha = softmax\left(g\left(BN\left(W_{att} \odot g\left(g(W_i \odot v_i^*) \oplus g\left(W_j \odot v_j^*\right)\right)\right)\right)\right) \quad (2)$$

where v_i' and v_i are updated output source nodes features and input source nodes features. hs represents the number of heads which is 8 heads in total implemented in the layer. g is the activation function which is softplus in this layer. $\odot$ represents the dot product operation between matrices or vectors, and $\oplus$ represents matrix or vector concatenation not addition. BN denotes a batch normalization layer. W_i and W_i are weights initialization for source nodes and neighboring nodes, respectively. W_{att} is the weights initialization for attention. v_i^* and v_j^* are augmented features vector and can be defined as

$$v_i^* = v_i \oplus (W_{i^*} \odot e_{ij} + b_{i^*}) \quad (3a)$$

$$v_j^* = v_j \oplus (W_{j^*} \odot e_{ij} + b_{j^*}) \quad (3b)$$

softmax is an activation function which is commonly used in deep learning. softmax exponentially normalizes the input vector. The formula for the softmax activation function is $\frac{e^{z_i}}{\sum_{j=1}^{K} e^{z_j}}$. In attention GNN layers, the softmax exponentially normalizes the input vector to give normalized weights for the nodes. The reason why the connecting lines between nodes vary in thickness as shown in Fig. 1 is because the layer informs the source node to pay more or less attention on a neighboring node. The source output node features from the multi-head augmented crystal attention are constructed by the previous node source node features -hence residual type of learning-combined with the attention from the neighboring nodes. The multi-head augmented crystal attention layer output is applied 3 times, and Relu activation function is applied to the multi-head augmented crystal attention layer output each time. Then, the atom attention layer can be defined by

$$v_i' = v_i + softmax\left(W_{atomAtt2}\left(BN\left(g\left(W_{atomAtt1}\left(v_i \oplus v_{iCgcnn}^*\right) + b_{atomAtt1}\right)\right)\right) + b_{atomAtt2}\right) \odot v_i = v_i + \alpha_{atom} \odot v_i$$
$$\alpha_{atom} = softmax\left(W_{atomAtt2}\left(BN\left(g\left(W_{atomAtt1}\left(v_i \oplus v_{iCgcnn}^*\right) + b_{atomAtt1}\right)\right)\right) + b_{atomAtt2}\right)$$
$$v_{iCgcnn}^* = g\left(W_{iCgcnn} \odot v_{iCgcnn} + b_{iCgcnn}\right) \quad (4)$$

The purpose of this layer is for the source nodes to pay attention to the initial weighted atom features which stem from the CGCNN features which is why α_{atom} weights go back to the same atom as shown by Fig. 1. Therefore, the initial weighted CGCNN atom features are weighted to update the input source node features coming from the multi-head crystal attention layer. Again, the thickness of the connection between the node to itself depends on the attention from α_{atom} weights. The updated source node features from the atom attention layer are equal to the source node features from the multi-head augmented crystal attention combined with the atom attention of weighted CGCNN features.

The following explains the layers and how they can help the model learn from the structures. The first layer is the convolution layer. The layer helps the source nodes from the edges receive messages from the target nodes (i.e., neighbors which include the neighbors from the other periodic cells). The messages from all the neighbors are summed into each source node (i.e., each atom in the original cell). As can be seen from both attention layers: mutli-augmented crystal attention layer and single head atom attention layer, the nodes embeddings get updated by summing the previous node embeddings and multiplying the previous node embeddings with the attention weights represented by "α". The α from the mutli-augmented crystal attention layer is obtained through getting features through concatenating embedding of augmented source and target nodes embeddings. The augmented node features (i.e., source or target nodes) are linearly transformed from concatenated gaussian expansion and node embeddings. The purpose of α in this layer is to assign varying degrees of importance based on the distance between the source and target nodes. Such node embedding updates can help the CATGNN model in analyzing the strength of interactions between the atoms based on the distance and node features. The α from the single head atom attention layer is obtained from the non-linearly transformed CGCNN features for each node. In this case, α attention weights are utilized to assign varying degrees of importance based on the CGCNN elemental features of each node. Such node embedding updates can help the CATGNN model in learning and adjusting the node embeddings based on their nonlinearly transformed elemental features. The mean pooling is performed on the node embeddings to average the contribution from all the nodes in the cell. After pooling, CATGNN makes the total phonon DOS prediction.

The training, validation, and testing data split with respect to the entire dataset (i.e., 4994 materials) is approximately 80 %/10 %/10 %, respectively, i.e., the number of materials in training, validation, and testing sets are 4,013, 482, and 499, respectively. The balance in training, validation, and testing datasets splitting is dictated by the elements. The data balance is performed for the structures that include each element from the 62 distinct elements in the dataset. For example, structures that contain the element Hydrogen (H) incorporate approximately 80 % of training, 10 % of validation and 10 % of testing datasets. For example, if the number of materials that contain hydrogen (H) is 100, then approximately 80 of those materials will be used for training, 10 for validation, and 10 for testing. Although such numbers are not always guaranteed, the numbers should be close to such splitting in terms of percentages or fractions. This way we will ensure that the distribution of elements in the training, validation, and testing datasets will be more or less the same to a large extent. Such data balance method

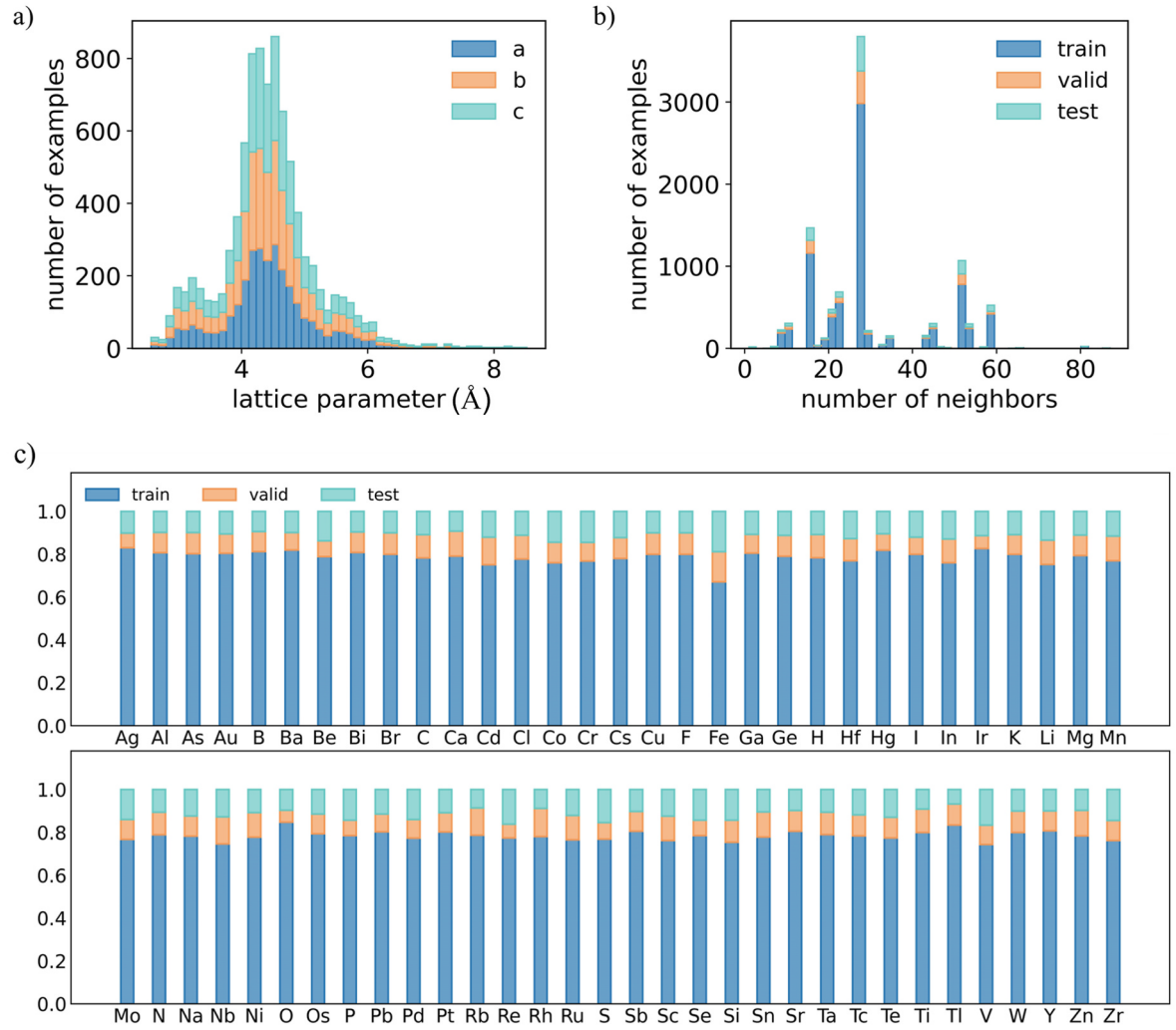

Fig. 2. a) Normalized and balanced training, validation, and testing splitting for all 62 elements from the dataset which ensures the balance in the dataset. b) A histogram of lattice constants (*a*, *b*, *c*) for the entire dataset. c) Training and validation loss curves in blue and yellow, respectively, in each epoch up to 150 epochs.

is confirmed by Fig. 2a which shows the percentage of structures for each element in training, validation, and testing datasets. This methodology of balancing the datasets is to ensure that the CATGNN model trains, validates, and tests the total phonon DOS using all types of elements. Balancing the dataset is necessary prior to training machine learning models in general to avoid biased dataset so that successful training on all possible scenarios can be ensured. Fig. 2a shows the normalized and balanced training, validation, and testing splitting among all elements. The columns that represent species are normalized to unity due to the unbalanced number of samples that contain each element. However, as long as the CATGNN model trains, validates, and tests on each element, we consider the dataset balanced. Herewith, executing a statistical analysis which outputs the number of samples (i.e., materials) with a particular range of lattice constants (*a*, *b*, and *c*) can help in understanding how the selected R_{max} capture the periodicity of atoms in other periodic cells. The statistical analysis for the lattice constants is shown in Fig. 2b. The *y*-axis in Fig. 2b shows the number of materials that have a lattice constant shown in the *x*-axis. The average lattice parameters in the following format (*a* / *b* /*c*) are 4.85/4.84/5.32 Å. The average lattice constants are not too large so a cutoff radius between 4 and 5 Å should be sufficient to capture the neighboring environment for each node and even capture the structures periodicity from other neighboring periodic cells. The loss criterion used in the model is the Mean Squared Error (MSE) at each iteration (i.e., epoch). The loss or MSE in the model is calculated based off the total DOS predicted by the model and compared with the "true" DFT calculated total DOS. After each total DOS prediction epoch, the loss is calculated, and the error backpropagates to update the embeddings, weights and biases in CATGNN layers. The model performance of the loss represented by MSE in training and validation datasets is shown in Fig. 2c by the blue training curve and orange validation curve. The training dataset loss decreases at each epoch and continues to decrease even though it looks like it plateaus. However, that is not the case with the validation dataset loss represented by the orange curve which seems to plateau around the 50th epoch. The total number of training epochs is 150. The AdamW optimizer is used in the model as an adaptive learning rate optimization algorithm at each epoch. The learning rate controls how much the embeddings can change which was taken to be 0.02 initially with a weight decay of 10^{-5}. However, the scheduler reduces the initial learning rate from 0.02 to 0.001 gradually and linearly up to the 100th epoch. Then, the learning rate stays at 0.001 till the 150th epoch. The batch size used in the training process is 256, i.e., 256 graphs or materials are trained at a time. We would like to point out that, training the CATGNN model for 150 epochs takes less than 2 h using 24 CPU cores. After training, the model on average takes less than 1 s to predict phonon DOS for a new material. In contrast, DFT takes exceedingly longer to calculate the 2nd order IFCs for one material which is used to obtain the phonon DOS. For example, calculating the phonon DOS for a cubic BN, which has high symmetry and low number of atoms in the primitive cell, requires 2 supercells with displaced atoms in the finite displacement method. The

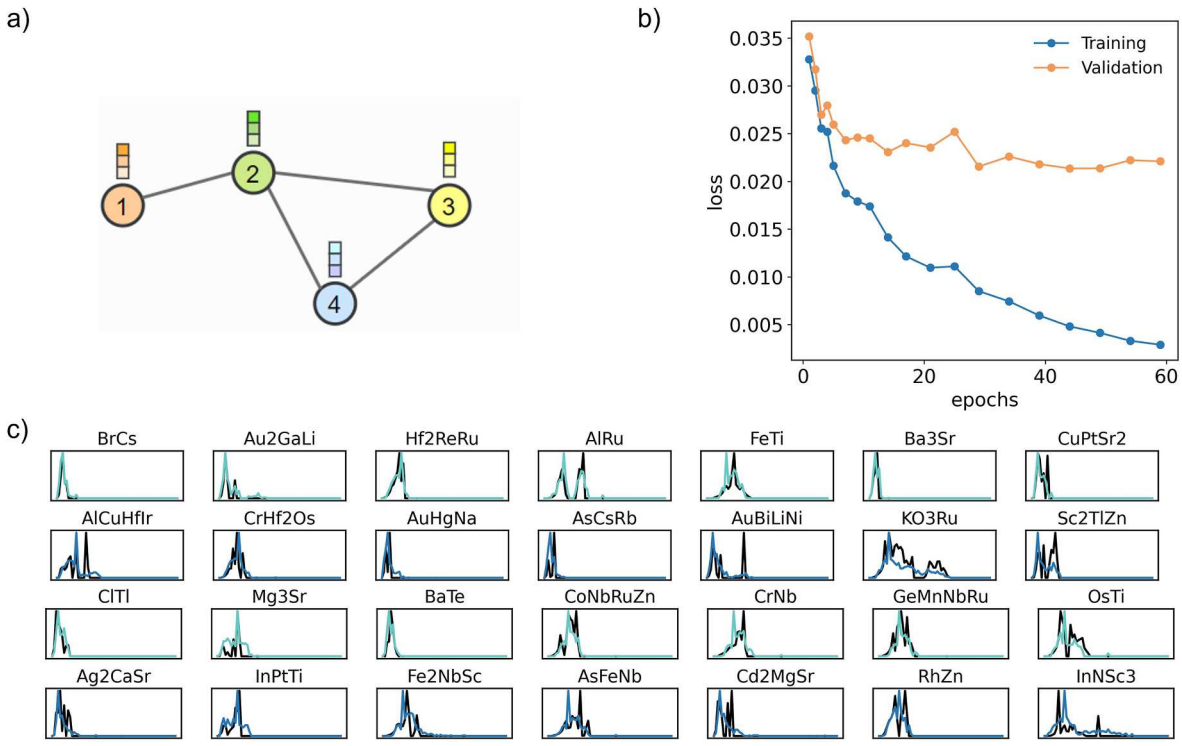

Fig. 3. Validation of trained CATGNN model by randomly selected materials. (Left panel) The MSE quartiles in the testing set of total phonon DOS. (Right panels) The black color represents the "true" total phonon DOS of the materials calculated by DFT whereas the other color represents the predicted total phonon DOS withing MSE quartiles regions of light green (0–0.25), blue (0.25–0.5), yellow (0.5–0.75), and light red (0.75–1).

computational cost of self-consistent field (SCF) DFT calculations for each supercell might take more than 2 h with 24 CPU cores. It will take much longer e.g. >10 h if the material contains heavier elements or the material has low symmetry and large number of atoms in primitive cell. Therefore, a rough estimate of the speedup of CATGNN as compared to SCF DFT would be on the order of 10^3–10^4.

It is worth noting that the total phonon DOS by PHONOPY are generated every 0.1 THz up to 40 THz i.e., the total frequency points in the phonon DOS curve (data) will be 400. Then we smoothened the phonon DOS by utilizing Gaussian smearing with sigma equal to 0.4 to take care of the peaks, which is an important step of the so-called "data cleaning". We have carefully tested the smearing parameter and finally identified a good parameter that gives out the best performance of our model training. After smoothening we output the phonon DOS data every 0.6 THz, so the length of the output array should be 67 for all the materials. In Fig. 3, the black colored curves represent DFT calculated total DOS. The cyan and blue colored curves are the predicted total DOS curves. It is seen from Fig. 3 that the predicted total DOS curves in the testing set are generally close to the DFT calculated DOS, and that proves the model's accuracy in predicting the total DOS of materials that the model was not trained on. The prediction of total DOS in the testing set materials seem to be precise enough to even capture the DFT total phonon DOS curves, peaks, and the location of those peaks. Since the error is different for each material, we divide the error of the material's total phonon DOS into MSE quartiles which are different from the total MSE from the total phonon DOS of all the materials (i.e., 0.012 which is higher than MSE of 0.015 from Ref. [28] model) in the testing set. The quartiles are represented by light green, blue, yellow, and light red, respectively. Most of the materials occur in the second quartile (i.e., blue). Upon looking at some of the total phonon DOS curves in that quartile, we see great matching between the black DFT total phonon DOS curve with the blue predicted curve by CATGNN. The MSE quartile with the second most common materials is the light green which also has the least MSE, and we see even more matching between the black DFT total phonon DOS curve with the light green curve predicted by CATGNN. The yellow color indicates the 3rd quartile which has the 3rd most materials among the rest of the quartiles. Although the MSE is larger compared to the previous two quartiles, the CATGNN predicted total phonon DOS curves also largely match the DFT results with minor deviations. The red color represents the 4th quartile with the highest MSE and least number of materials. The phonon DOS of some materials that contain light elements (e.g., H) such as Ca_2H_6NiPt have low MSE, but some materials phonon DOS that contain H have higher MSE such as ClH_3Sr_2. Similar phenomenon was found in Ir-containing structures such as $Hg_2Ir_4S_8$ and $Ir_4Na_4O_4S_4$ with low and high MSE, respectively. Through these observations, high MSE in the model is not caused by the existence of light or heavy elements in the materials. High MSE might have been caused by the model not being sufficiently good to learn the peaks of phonon DOS, which could be one of the major reasons for the model not being able to predict phonon DOS well. In addition, the local atomic environment varies for some specific elements which could also cause the phonon DOS to vary. The result indicates that most of the materials in the testing set are predicted phenomenally well by CATGNN. The CATGNN predicted red curves are not largely off from the black DFT total phonon DOS curves, except for some peaks in ClH_3Sr_2. Our CATGNN model can also distinguish between materials with heavy elements and light ones which is important for phonon related applications, since materials with light element tend to have total phonon DOS at higher frequencies and materials with no light elements do not have total phonon DOS at high frequencies [66]. CATGNN predicted the total phonon DOS of Ca_2H_6NiPt that contains a light element of H extraordinarily well although it contains other heavy elements and several peaks as well. CATGNN also accurately predicted total phonon DOS of $IrRe_3$ which contains heavy elements.

b) Screening substrates for cooling high electron mobility transistors by phonon DOS overlap

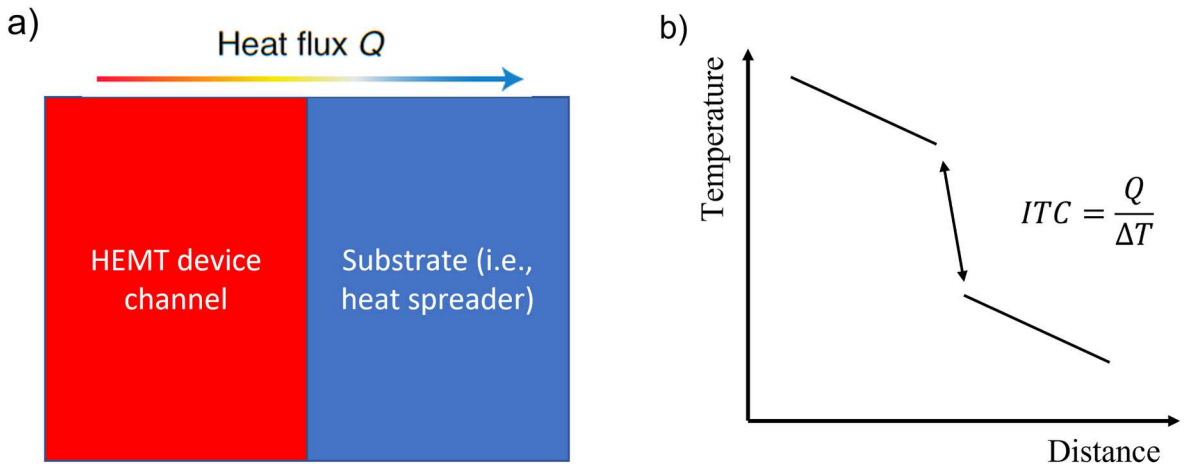

Fig. 4. a) A schematic outline on how the heat dissipates from the HEMT device channel into the substrate (i.e., heat spreader). b) Overall schematic of representative temperature profile on how to calculate interfacial thermal conductance (ITC) from Monte Carlo simulation outputs using heat flux and temperature difference at the interface.

Table 1
Candidate materials (in alphabetical order) with high LTC to be analyzed for HEMT devices. The structure ID and bandgap information is obtained from the OQMD database [8].

OQMD ID	Formula	Bandgap (eV)	LTC (W/mK) at 300 K	Heat source/sink classification
1218324	AlN	3.458	272.93 (high)	Heat source or sink
8235	BAs	1.416	2358.3 (ultrahigh)	Heat sink
1218562	BN	4.795	839.28 (ultrahigh)	Heat source or sink
5664	BP	1.367	532.39 (high)	Heat sink
1218583	BSb	0.81	420.02 (high)	Heat sink
1215492	$C_{diamond}$	4.4	2966 (ultrahigh) [81]	Heat sink
1222562	c-GaN	2.026	199.27 (high)	Heat source or sink
1472729	h-GaN	2.2	335.37 (in-plane) and 316.29 (out-of-plane) (high) [82]	Heat source or sink
4566	SiC	1.586	470.57 (high)	Heat sink

HEMTs are outstanding devices for high-frequency and high-power applications [71–73]. Hexagonal GaN (h-GaN) is one of the most common and crucial materials in HEMT applications due to its desirable attributes, such as medium to high LTC, high electron mobility, wide bandgap, and high breakdown electric field [45,46]. However, some of the issues that HEMT devices encounter are current leakage [74,75] and heat dissipation limitations from the excessive heating which cause large increase of temperature in the device channel [45]. Electric current leakage is normally solved using materials with large bandgap or various materials combinations of metal-insulator-semiconductor HEMT [76]. The heat dissipation issues in high power electronics are often solved using high ITC between the layers to dissipate the excessive heat more effectively and thus reduce the temperature increase in the device channel. Several materials have recently emerged with potential applications in HEMT device channels along with h-GaN, such as AlN [77] and BN [78]. It was also reported that cubic GaN (c-GaN) was used in HEMTs [79,80]. Here we calculate ITC and analyze several combinations of heat sources and heat sinks from previously unexplored materials, based on the phonon DOS predicted using the trained CATGNN model. Here we consider the effect of total phonon DOS on ITC. Further ITC analysis demonstrates that our model can accurately predict phonon DOS of new structures, and the predicted total phonon DOS can further explain most of ITC results associated with HEMT devices.

Fig. 4a illustrates how heat flows from the channel in HEMT device to the substrate that acts as a heat source. ITC plays a significant role because if the ITC is low, heat will not dissipate at a sufficient rate which poses temperature limitations to HEMT and eventually degrades the performance of HEMT devices. Fig. 4b shows the schematic of a representative temperature profile of a HEMT interface and how to calculate ITC using necessary outputs such as heat flux and temperature drop from the hot source to the cooler substrate at the interface. Table 1 shows several materials with high LTC from the dataset used to train the phonon DOS. Materials with high LTC are selected because they possess weak phonons anharmonicity, and they are traditionally considered to be promising candidates as heat sinks. For example, diamond is considered in this analysis because it is used in many HEMT devices as a heat sink or substrate [45–48]. Such materials were involved in ITC calculations since they were considered in multiple HEMT studies as previously stated.

With the obtained 2nd and 3rd order IFCs, we utilize almaBTE [58] to approximate the interfacial phonon transmission coefficient in DMM and calculate the heat flux and temperature drop across the interface between the heat source and heat sink (substrate). almaBTE utilizes the Monte Carlo simulations to help calculate ITC at the interface when phonons dominate interfacial thermal transport [58]. The DMM assumes that phonons lose memory of the state after reaching the interface. Once the phonons reach the interface, they either scatter back into the initial material or the subsequent medium. Whether the phonon scatters back or transmits into another medium depends on the phonon DOS of the two contacting materials [83]. The phonons will scatter into the same energy phonon state in either medium, which implies that the transmission probability of the phonon states with the same frequency is the same. The ITC for a phonon with frequency ω and mode j transmitting from material A to material B [84] can be defined as:

$$ITC = \frac{1}{4}\sum_j \int_0^{\omega^{\nu}_{A,j}} D_{A,j}(\omega)\frac{\partial n(\omega,T)}{\partial T}\hbar\omega v_{A,j}\alpha_{A\to B}(\omega)\, d\omega \quad (5)$$

where ω^{ν} is the cutoff frequency, $D(\omega)$ is the phonon DOS, and $\alpha_{A\to B}$ is the transmission coefficient from material A to B which is defined by the DMM model as

$$\alpha_{DMM,A\to B} = \frac{\sum_j D_{B,j} v_{B,j}}{\sum_j D_{A,j} v_{A,j} + \sum_j D_{B,j} v_{B,j}} \quad (6)$$

where v is the phonon group velocity. To calculate heat flux, almaBTE [58] divides the 200 nm thick heterogeneous material into 300 bins. The temperature deviation in bin l for a particle moving from depth x_i at time

t_i to depth x_f at time t_f is calculated by

$$\frac{1}{wC_l}(t_f - t_i)\rho\frac{|\Delta x_l|}{|x_f - x_i|} \tag{7}$$

where w is the bin width, C_l is volumetric heat capacity, and ρ is deviational intensity for each particle. The deviational intensity for each particle is defined by

$$\rho = \pm\frac{|\mathfrak{T}_{hot}| + |\mathfrak{T}_{cold}|}{N_{particles}} \tag{8}$$

where $\mathfrak{T}$ is isothermal reservoir and the sign ($\pm$) depends on the isothermal reservoir that emitted the particles. The isothermal reservoir is defined as

$$\mathfrak{T}_{iso} = \frac{\hbar}{V}\sum_k (v_k \cdot n)\, H(v_k \cdot n)\, \omega_k \left[f_{BE}(\omega_k, T_{iso}) - f_{BE}(\omega_k, T_{ref})\right] \tag{9}$$

where v_k is group velocity at wavevector k, n is normal vector, H is Heaviside function, ω_k is angular frequency at wavevector k, f_{BE} is Bose-Einstein distribution of phonons, T_{ref} is reference temperature ($T_{ref} = \frac{T_{hot}+T_{cold}}{2}$). The heat flux in each bin is calculated by accumulating $\pm\rho/L_{tot}$ each time a trajectory segment traverses the bin center. The sign ($\pm$) depends on the particles' movement: (+) if hot-to-cold or (−) if cold-to-hot. Even though the spectral heat flux equation is not explicitly written in Ref. [11], it is obtained by the particles' angular phonon frequency they are associated with and the moment they cross a bin as shown in Fig. 4b. After obtaining the heat flux, onc can calculate ITC by dividing the heat flux by the temperature change at the interface. The DMM was originally developed to predict ITC in Helium in contact with other solid interfaces [85] but was later used to predict ITC in other systems [86]. It is worth mentioning that the DMM model does not consider the details of the interfacial structure, such as roughness, interatomic bonding, residual strain, etc. Precisely determining ITC requires very computationally expensive simulations, such as nonequilibrium molecular dynamics (MD) simulations which consider both harmonic and anharmonic phonon scattering [87,88] and Green's function method [89,90] where full phonon anharmonicity is challenging to consider. However, the MD simulations would require accurate and fast interatomic potentials for many different materials and diverse interfacial structures. Even for recently developed so-called universal machine learning potentials, their accuracy and effectiveness to interfacial structures are still unknown. Despite the shortcomings of DMM [91], it remains a useful tool for capturing the trends in phonon transmission across interfaces [92] and it provides a reasonably accurate yet fast approach for quick screening materials for interfacial thermal transport. Moreover, the above more accurate approaches to calculate ITC still depend on phonon DOS overlap from fundamental physics point of view, and therefore using our developed CATGNN to down select materials with high phonon DOS overlap with target source materials remains a good initial screening strategy for other more accurate approaches. A more sophisticated workflow that combines fast screening of candidates using CATGNN model and subsequent fine filtering and validation by MD simulations will be our future work.

A good first approximation condition to having a high ITC in DMM at the heat source/sink interfaces has long been thought to be possessing large overlap between the phonon DOS of the two materials [93–99]. The formula for phonon DOS overlap is defined as follows

$$\text{Phonon DOS Overlap} = \frac{2\int_0^\infty D_{overlap}(\omega)d\omega}{\int_0^\infty D_{heat\ source}(\omega)d\omega + \int_0^\infty D_{substrate}(\omega)d\omega} \tag{10}$$

where $D(\omega)$ represents the phonon DOS of a material, and ω is the phonon frequency. The unit of phonon DOS is 1/THz or THz^{-1}, while the phonon DOS overlap is unitless as can be deduced from equation (10). The previous equation is suggested to help screen materials candidate pairs with potentially high ITC since it can be observed that it is close to the transmission coefficient equation formulation. ITC was calculated for the interface between two layers with 100 nm thickness for each layer. ITC results between the heat source materials (i.e., AlN, BN, c-GaN, and h-GaN) and the heat sink materials from Table 1 are shown in Tables S1–S4 in Supplemental Information. The heat sources AlN, BN, and c-GaN are isotropic, but h-GaN is anisotropic. Therefore, ITC should not depend on orientation in AlN, BN, and c-GaN. For anisotropic h-GaN, we performed additional almaBTE runs by using different crystal orientations. The results shown in Table S5 in Supplemental Information reveal that the ITC with materials contacting in different crystalline directions are different, but the values do not differ too much. That can be mainly explained by the low difference in the LTC of h-GaN among three directions. Some difference can be also explained by the stochastic nature of Monte Carlo simulations in almaBTE that produce slightly different results in different runs. Overall, the orientation of the crystal can take effect through group velocity in the ITC calculation as indicated in Eq. (5). Each table has 5 columns: (1) various heat source–heat sink combinations with one HEMT material for each table, (2) OQMD ID for the heat sink, (3) LTC for heat sink, (4) phonon DOS overlap between the heat source and heat sink calculated by Eqs. (10), and (5) ITC between heat source and heat sink. The tables present the results for all high LTC materials in Table 1 regardless of the phonon DOS overlap. Furthermore, Tables S1–S4 in Supplemental Information give out the ITC for other substrates with lower LTC and possibly higher phonon DOS. The objective is to see how ITC varies with diverse LTC (i.e., high, moderate, or low LTC) when the phonon DOS overlap is also varying between the heat source and substrate. Note that all ITC are calculated at 300 K because we believe many relevant applications such as heat dissipation for HEMT devices are near room temperature. We have not investigated ITC of the studied heat sources at higher temperatures yet, but ITC at higher temperatures is certainly worth being investigated. With interatomic force constants available, it is straightforward to extend the current ITC calculation to higher temperatures. Covering phonon transport at high temperatures will be one of the major tasks in the near future.

Fig. 5 shows 3D visualization of the ITC results with AlN, BN, c-GaN, and h-GaN as heat source in HEMT. The corresponding substrate LTC, detailed ITC values, and phonon DOS overlap for all cases reported can

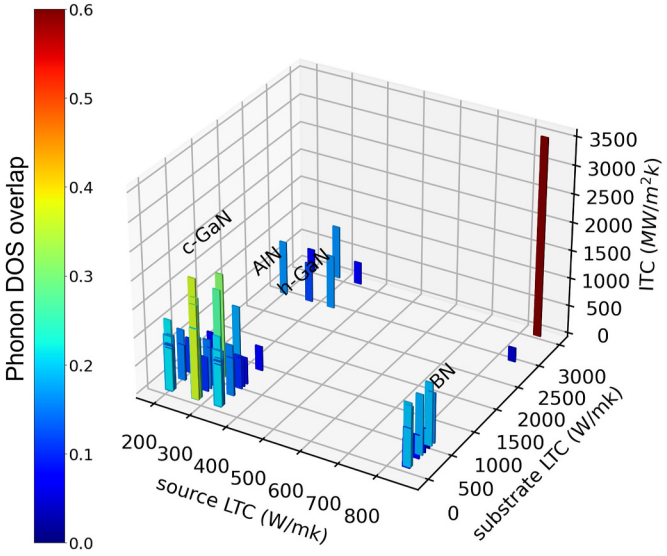

Fig. 5. 3D bar plot for all ITC results using AlN, BN, c-GaN, and h-GaN as heat source in HEMT. The height of the bar reflects the magnitude of ITC, while the color bar represents the phonon DOS overlap between heat source and heat sink (substrate). The corresponding substrate LTC, detailed ITC values, and phonon DOS overlap can be found in Tables S1–S4 in Supplemental Information.

be found in Tables S1–S4 in Supplemental Information. The height of the bar in Fig. 5 reflects the magnitude of ITC values, while the color bar represents the phonon DOS overlap between heat source and heat sink (substrate). The results are grouped into 4 islands, corresponding to AlN, BN, c-GaN, and h-GaN as labeled as heat source. Most of the heat sinks or substrates have medium to low LTC and only a few have ultrahigh LTC. The top two materials in terms of substrate LTC are $C_{diamond}$ and BAs. The highest bar, i.e., the highest ITC of 3542 MW/m^{2}K, occurs at BN-$C_{diamond}$ interface as denoted by the dark brown color, with corresponding highest phonon DOS overlap of around 0.6. Many other interface combinations possess ITC over 1000 MW/m^{2}K and those are listed in detail in Tables S1–S4 in Supplemental Information Fig. 5 also illustrates that, medium to high ITC does not always occur at two materials with high LTC. Indeed, we found many high ITC interfaces, but the two constitutive materials only have medium LTC, such as those in the left-bottom corner of Fig. 5. For instance, h-GaN/BSb interface possesses a moderate ITC of 598 MW/m^{2}K although their phonon DOS overlap is high (0.51) and LTC is also high for both materials (316.29 and 420.02 W/mK for h-GaN and BSb, respectively). This result also confirms that the high phonon DOS overlap, or vibrational similarity between two materials in contact does not necessarily lead to high ITC.

More rigorous analysis for the correlation between ITC and phonon properties of component materials relies on the numerical simulation results of large number of structure pairs. To this end, we performed additional DFT calculations by randomly selecting a few hundred new structures from the prediction structure pool and calculated the IFCs of these structures. We further calculated their phonon DOS, the DOS overlap with representative heat sources, and the ITC of the corresponding interfaces. These additional calculations raise the number of materials between 900 and 1000 for each heat source. The visual portrayal of the correlation between ITC and phonon DOS overlaps along with other phonon properties of the component materials are shown in Fig. 6. It is worth mentioning that, for best illustration of strong correlation, we have tried a few different material properties as the second dependent variable, i.e., the color coding in Fig. 6, including LTC of heat sink materials (see Fig. S5 in Supplemental Information). We finally choose the product of average group velocity from the acoustic branch of the heat source and heat sink (denoted as $\overline{GV_1}$ and $\overline{GV_2}$, respectively) of the phonon DOS overlapping region for the color bar in Fig. 6, as it reflects the best correlation of the data presented herein. Here, the average acoustic branch $\overline{GV_1} \times \overline{GV_2}$ is calculated as

$$\overline{GV_{1\ ac}} \times \overline{GV_{2\ ac}} = \frac{\sum_{f_1}^{f_2} \nu_1}{n_1} \times \frac{\sum_{f_1}^{f_2} \nu_2}{n_2} \tag{11}$$

where the subscripts "1" and "2" refer to material 1 and 2, respectively, "ac" denotes acoustic branch, ν_1 and ν_2 are the corresponding group velocity values for material 1 and 2, respectively, obtained from the acoustic branch phonon modes from the phonon dispersions within the cutoff frequencies f_1 and f_2 in which the phonon DOS of the two materials overlap, n_1 and n_2 are the total number of those acoustic branch phonon modes in the overlap window. The product of average group velocity of the heat source and heat sink as defined by Eq. (11) provides a measure of thermal transport properties in the overlapped phonon DOS frequency ranges and distinguish the performance of heat sinks with high average group velocity from the ones with low group velocity. Multiple mechanisms affect thermal transport across the interface in

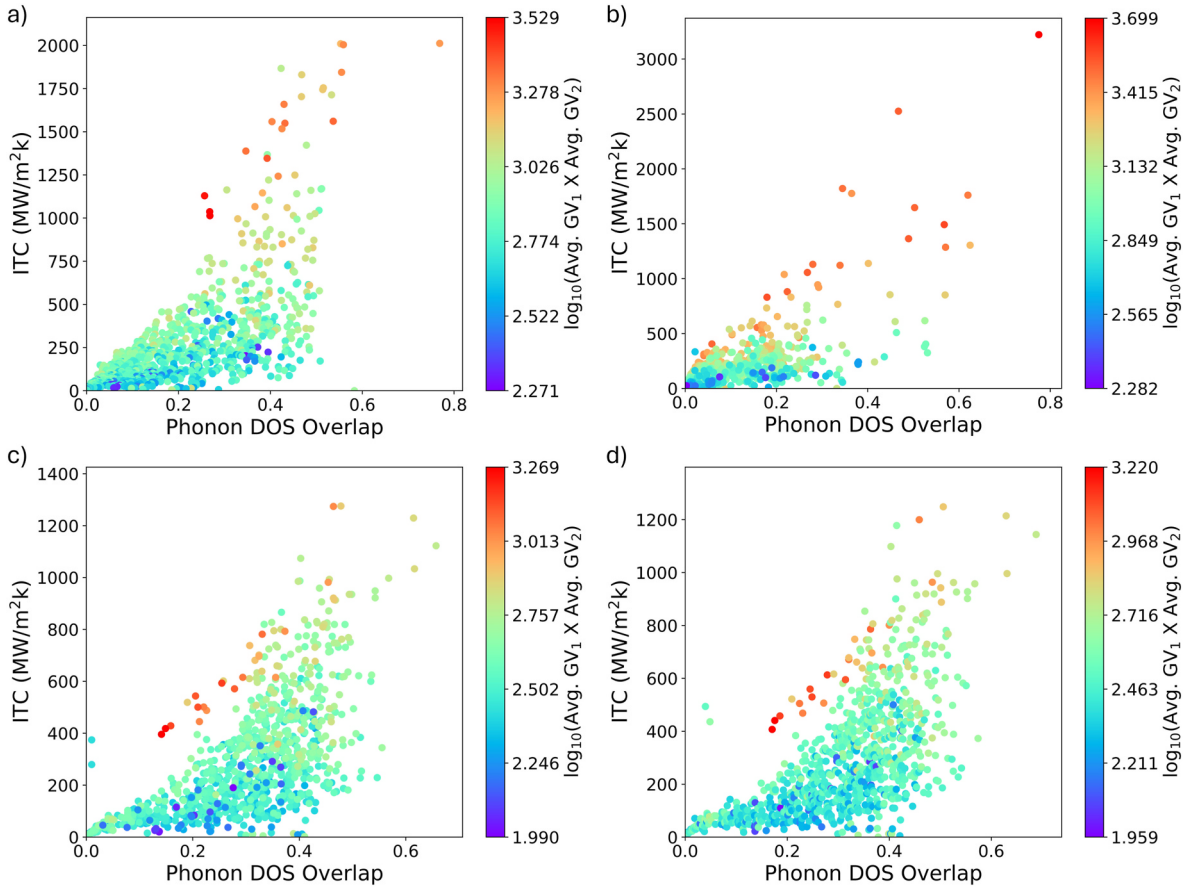

Fig. 6. ITC vs. phonon DOS overlap between the heat source a) AlN, b) BN, c) c-GaN, and d) h-GaN and various heat sink substrates. The color bar indicates the product of average group velocity of the acoustic branches of heat source and heat sink $\log_{10}(\overline{GV_1} \times \overline{GV_2})$ in the overlapping phonon DOS frequency range for the formed interfaces.

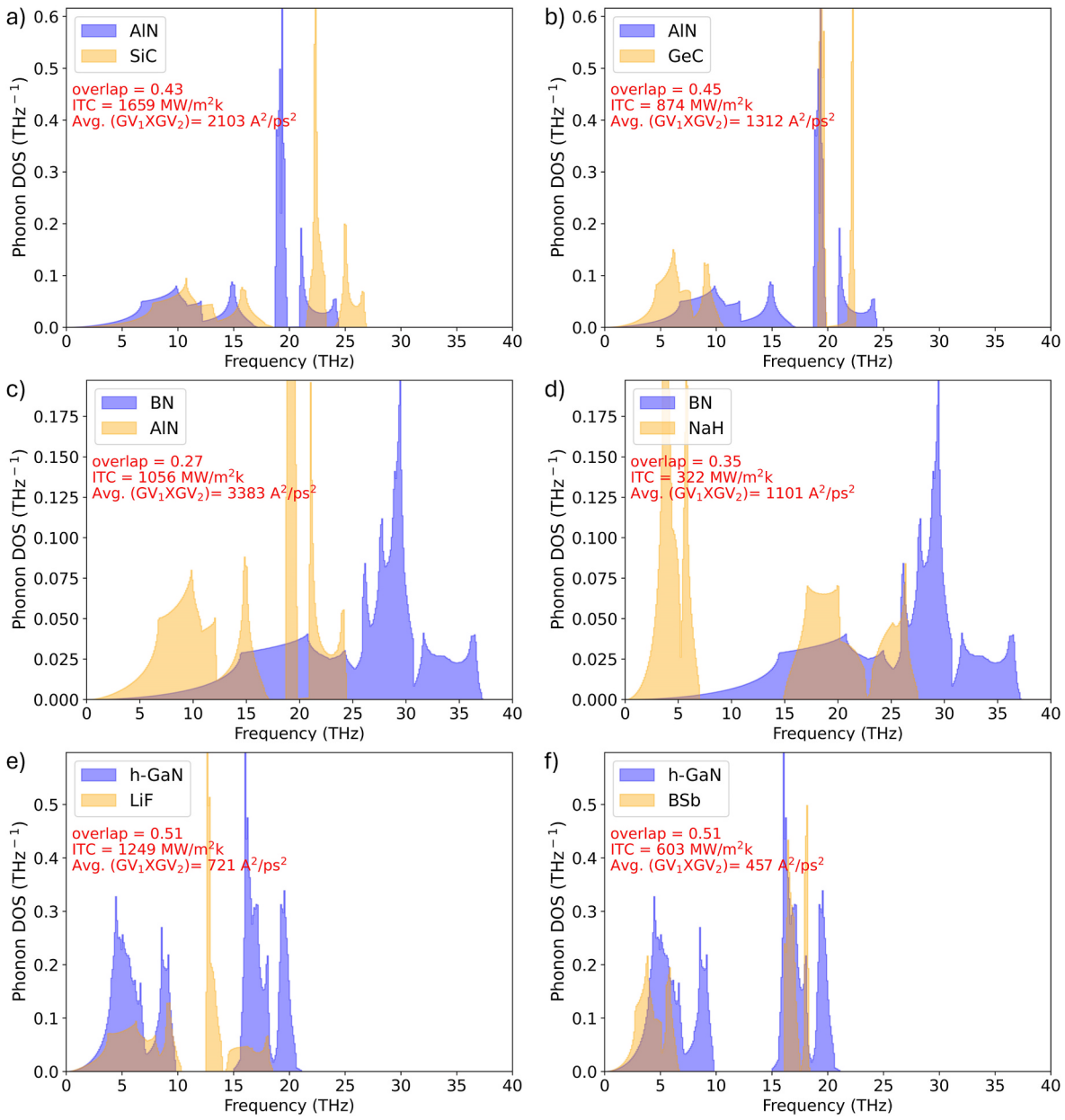

Fig. 7. Phonon DOS overlap between HEMT materials with various substrates. a) AlN/SiC, b) AlN/GeC, c) BN/AlN, d) BN/NaH, e) h-GaN/LiF, and f) h-GaN/BSb. The left panels represent high ITC of the formed interfaces, while the right panels represent low ITC, but both panels have similar phonon DOS overlap (labeled by red numbers). The phonon DOS of heat source and heat sink are represented by the light-blue and light-yellow, respectively, while the gray area represents the phonon DOS overlap between the heat source and heat sink. The phonon DOS overlap and the product of average group velocity of the acoustic branches of heat source and heat sink ($\overline{GV_1} \times \overline{GV_2}$) in the overlapping phonon DOS frequency range for the formed interfaces are indicated by red numbers.

terms of almaBTE simulation such as intrinsic, interface, and absorption phonon scatterings. However, group velocity plays a major role in ITC in DMM [83–92] which is why we suggested the product of average group velocity of the acoustic branches of heat source and heat sink as major structure features in terms of high ITC. However, this does not guarantee the ITC will be high for all cases with high product of average group velocity of the acoustic branches of heat source and heat sink, and vice versa. We anticipate that the reason for exception cases might stem from the interface phonon scattering predicted by the DMM model where the detailed phonon band structures of both heat source and heat sink get involved in a complicated way but are simply treated in DMM model. The reason why the group velocity is only considered in the acoustic branch is because of the insignificant contribution of the heat flux transported across the interface from the optical branches, due to their usually low phonon group velocities, as can be seen and confirmed from Fig. 7 as well. The analysis shown in Fig. 6 is performed on almost 1000 materials by DFT calculations and can provide clear insights on interfaces with various values of phonon DOS overlaps and average group velocities in the acoustic branch. Similar analysis is performed on LTC of heat sinks, which is shown in Fig. S5 in Supplemental Information to give more insights on what makes an interface have a high ITC. The advantage of using CATGNN for computing ITC is to screen the phonon DOS overlap from large number of unknown potential candidates. Even though CATGNN cannot predict the group velocity so far, the initial accelerated screening of phonon DOS will be extremely helpful due to the direct correlation between phonon DOS overlap and ITC as evidenced by Fig. 6. Moreover, we would like to emphasize that, generally speaking, the group velocity is a 2nd order physical quantity that is easy

to train by various machine learning models including the state-of-the-art graph neural networks, like other 2nd order mechanical properties as we did before by global attention graph neural network such as bulk modulus and shear modulus [20]. Then, in principle we believe our CATGNN model can also be used for training and predicting group velocity. Future work will be done by training and predicting phonon DOS and group velocity simultaneously to make smooth and robust workflow for screening ITC.

The first clear trend shown in all panels in Fig. 6 is that ITC approaches zero when phonon DOS overlap approaches zero. This result is consistent with DMM model and mathematically accurate from Eqs. (5) and (6). Second, from Fig. 6, it is observed that as phonon DOS overlap increases, ITC in general increases, but has an interesting divergent behavior. The higher the phonon DOS overlap, the larger diversity the predicted ITC. The divergent behavior can be understood clearly from the panels through color mapping. If the phonon DOS overlap is in the medium or high range, but the average $\overline{GV_1} \times \overline{GV_2}$ is low (i.e., blue color region in the color bar), then ITC should be low as well. The opposite is also true, i.e., high phonon DOS overlaps with high average $\overline{GV_1} \times \overline{GV_2}$ should yield a high ITC. In contrast, this is not so obvious when using LTC of heat sinks as color mapping (see Fig. S5 in Supplemental Information). Some interesting results with high ITC that can be observed in Fig. 6 include AlN/BN interface with low phonon DOS overlap of 0.26 and ultrahigh ITC of 1037 (MW/m^{2}K), AlN/ScN with medium phonon DOS overlap 0f 0.37 and ultrahigh ITC of 1066 (MW/m^{2}K), BN/MgO with medium phonon DOS overlap of 0.22 and ultrahigh ITC of 1038 (MW/m^{2}K), and h-GaN/MgO with phonon DOS overlap of 0.33 and high ITC of 747 (MW/m^{2}K). These results suggest a route for searching for high ITC interfaces by using medium phonon DOS overlap but possessing high average acoustic group velocity product ($\overline{GV_1} \times \overline{GV_2}$) in the phonon DOS overlap frequency range. The same trend occurs for the medium to low LTC materials whose interfaces do not always result in low ITC. Some medium to low LTC materials could also have ultrahigh ITC, such as BN/MgO (1044 MW/m^{2}K), h-GaN/LiF (1237 MW/m^{2}K), and h-GaN/ZnO (1016 MW/m^{2}K). The same phenomenon was observed experimentally in Ref. [97]. The ITC for TiN/AlN interface can reach as high as 800 MW/m^{2}K, while the LTC of TiN is only 16 W/mK. Also, there are some materials with low to medium LTC, such as ZnO (~50 W/mK averaging over all directions), MgO (~30 W/mK), HfN (~14 W/mK), but their associated interfaces possess ITC on the order of a few hundred MW/m^{2}K [100].

It is worth pointing out that, since the ITC values are approximately calculated by the empirical DMM model in terms of the interfacial transmission coefficients, there could be some so-called "outliers" coming out from the workflow. We have checked our data and indeed found some exceptions. For example, AlN/SrH_2 has ITC of 93 MW/m^{2}K even though the interface has phonon DOS overlap of 0.34 and $\log_{10}(\overline{GV_1} \times \overline{GV_2})$ of 2.91 $\log_{10}$(Å^2/ps^2), whereas AlN/$RbCaH_3$ has lower phonon DOS overlap of 0.28 and lower $\log_{10}(\overline{GV_1} \times \overline{GV_2})$ of 2.47 $\log_{10}$(Å^2/ps^2) but surprisingly a few times higher ITC of 418 MW/m^{2}K. Moreover, h-GaN/Li_2S has ITC of 143 MW/m^{2}K with phonon DOS overlap of 0.38 and $\log_{10}(\overline{GV_1} \times \overline{GV_2})$ of 2.5 $\log_{10}$(Å^2/ps^2), but h-GaN/PbS has higher ITC of 255 MW/m^{2}K even with lower phonon DOS overlap of 0.33 and lower $\log_{10}(\overline{GV_1} \times \overline{GV_2})$ of 2.2 $\log_{10}$(Å^2/ps^2). Even with such exceptions, the trend can be viewed clearly from the data that for the same phonon DOS overlap value, as $\log_{10}(\overline{GV_1} \times \overline{GV_2})$ increases, ITC generally increases, and vice versa.

Regarding the group velocity descriptor, for some materials, a range of phonon frequencies with high DOS but low group velocities may contribute comparably to a range of (acoustic) phonon frequencies with low DOS but high group velocities. Rigorously speaking, there is so-called frequency dependent accumulative ITC associated with this, which can be obtained by post-processing the simulation data such as in almaBTE, similar to the frequency dependent accumulative LTC of single crystals obtained from phonon BTE calculation. From such curve, one can find out the dominant frequency range where heat energy is transmitted most efficiently across the interface, and such dominant frequency range should be material dependent. However, all these detailed or bottom-level information cannot be easily obtained in a high-throughput manner, as one must fully calculate the IFCs of two materials first and then solve BTE for phonon transport across the interface formed by these two materials. Instead, here we use the acoustic phonon frequency as cutoff frequency as a fast and robust approach, and we find that this choice shows excellent performance to represent the strong correlation between ITC and fundamental and more importantly easy-to-obtain physical properties for the majority of material interfaces we analyzed. Fig. 6 supports our above statements since it shows a clear trend among ITC, phonon DOS overlap, and our average group velocity descriptor. Our descriptor clearly explains the deviation of ITC at each phonon DOS overlap value.

It is well known that the phonon DOS overlaps affect how the heat fluxes travel across the interface between the heat source material and substrate [91–96]. Fig. 7 displays the phonon DOS overlap of some selected combinations of heat source materials and substrates. The heat source/substrate pairs are selected based on high and low ITC values for each heat source material except for c-GaN which is not shown here because it has a substantially similar phonon DOS behavior to h-GaN. For brevity, we only show phonon DOS overlap for h-GaN as the heat source with other substrates. Fig. 7 demonstrates the cases of similar phonon DOS overlap but with distinct ITC values for each heat source material, where the phonon DOS of heat source and substrate are represented by the light-blue and light-yellow colors, respectively, and their phonon DOS overlap regions are indicated by the gray area. Fig. 7a exhibits high phonon DOS overlap of 0.43 at AlN/SiC interface with ITC of 1659 MW/m^{2}K (also see Table 1 in Supplemental Information). Fig. 7b shows a similar phonon DOS overlap value of 0.45 in AlN/GeC but with an ITC of 874 MW/m^{2}K which is approximately half of AlN/SiC shown in Fig. 7a. The explanation for the previous results in the AlN heat source cases is explicitly stated from Fig. 6, ie., higher average $\overline{GV_1} \times \overline{GV_2}$ in the acoustic branches in AlN/SiC yields higher ITC compared to that of AlN/GeC. In Fig. 7c, the interface of BN/AlN has a phonon DOS overlap, ITC, and average $\overline{GV_1} \times \overline{GV_2}$ as 0.27, 1056 MW/m^{2}K, and 3383 A^2/ps^2, respectively. However, BN/NaH interfaces in Fig. 7d shows a higher phonon DOS overlap of 0.35 with a significantly lower ITC of only 322 MW/m^{2}K which can be explained by the lower average $\overline{GV_1} \times \overline{GV_2}$ in the acoustic branches of 1101 A^2/ps^2. h-GaN/LiF in Fig. 7e and h-GaN/BSb in Fig. 7f have the same phonon DOS overlap of 0.51. However, the ITC in h-GaN/LiF is 1249 MW/m^{2}K which is roughly twice the ITC of 603 MW/m^{2}K for h-GaN/BSb. The disparity in ITC is elucidated by the higher average $\overline{GV_1} \times \overline{GV_2}$ in the acoustic branches in h-GaN/LiF of 721 A^2/ps^2 compared to 457 A^2/ps^2 in h-GaN/BSb. The results illustrated in Fig. 7 further confirm the strong positive correlation between ITC and average $\overline{GV_1} \times \overline{GV_2}$ of the acoustic branches in the overlap frequency range.

c) Spectral heat flux analysis of selected interfaces

Fig. 8 shows how the spectral heat flux varies along the distance of heat source and substrate with respect to the phonon frequency. The colormap represents the magnitude of the heat flux transported which has various ranges depending on the LTC of the materials in contact, where the red and blue colors denote high and low heat flux, respectively. The heat flux is extremely high in the overlapping regions of phonon frequencies between 3.8 and 12 THz in AlN/SiC as shown in Fig. 8a. Although another region of phonon DOS overlap between 21 and 24 THz exists in AlN/SiC as shown from Fig. 7a, that overlap does not seem to contribute significantly to ITC. For AlN/GeC interface, the frequencies from 3 to 10 THz show a high heat flux transport, which is exactly where the phonon DOS overlap occurs as seen from Fig. 7b. Another phonon DOS overlap occurs in 19–23 THz, but it does not

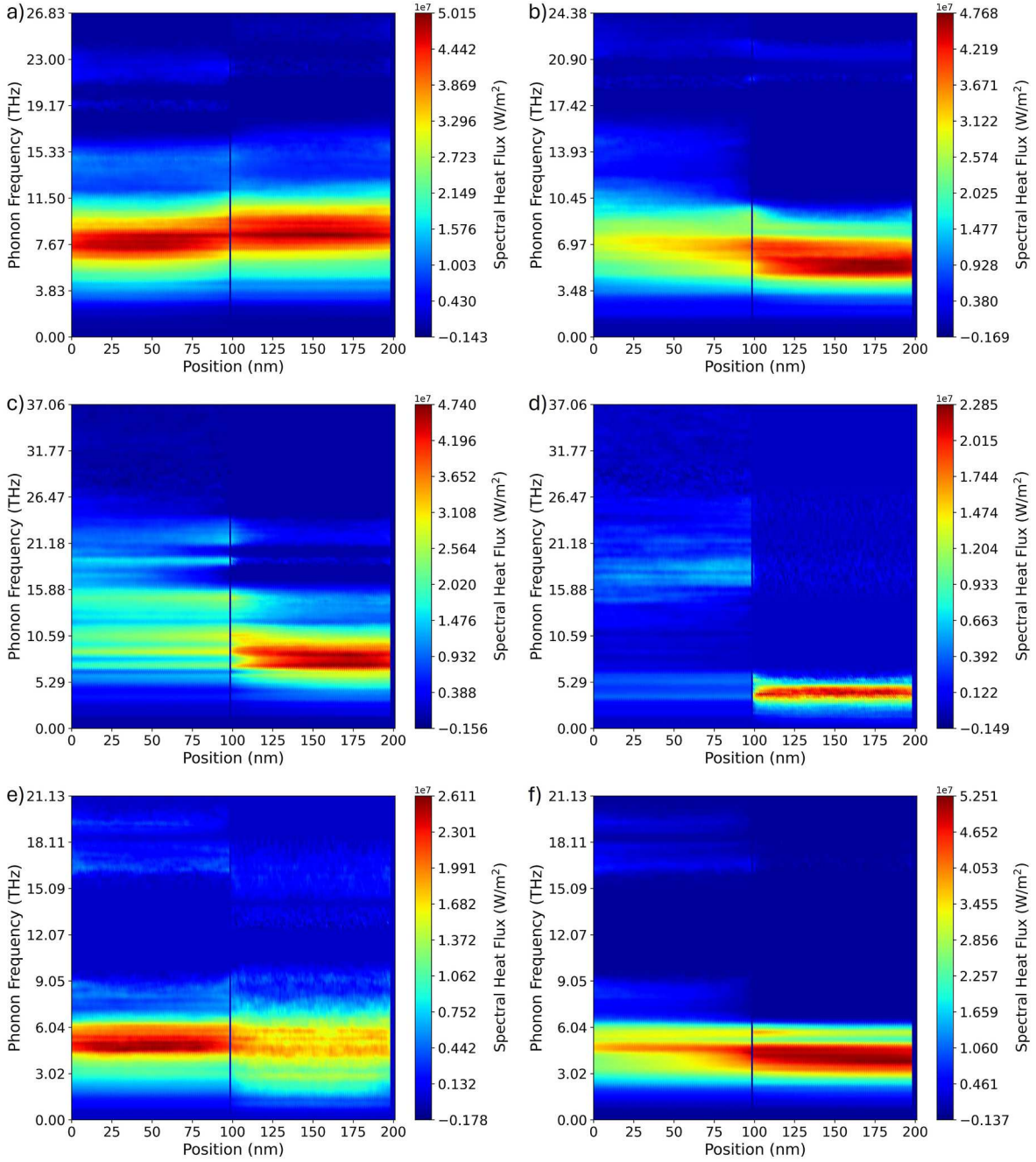

Fig. 8. Spectral heat flux at the interfaces corresponding to the cases in Fig. 7 a) AlN/SiC, b) AlN/GeC, c) BN/AlN, d) BN/NaH, e) h-GaN/LiF, and f) h-GaN/BSb. The red and blue color indicate the high and low heat flux transported by the specific frequency phonon modes, respectively.

transport high heat flux as indicated by the blue color in Fig. 8b. As for the heat source BN, Fig. 8c shows the high heat flux transported at 5 to 15 THz at BN/AlN interface which is where the phonon DOS overlap occurs as illustrated in Fig. 7c. Another phonon DOS overlap occurs between 19 and 25 THz in the optical branches but does not transport high heat fluxes. For BN/NaH, Fig. 8d shows higher heat flux between 3 and 5 THz (acoustic phonons for BN) where the phonon DOS overlaps, while the overlap in the optical branches does not transport the heat flux much. One more result that deserves attention is the maximum heat flux of 47 MW/m^2 in BN/AlN which is higher than the maximum heat flux of 23 MW/m^2 in BN/NaH. The higher heat flux transported in BN/AlN is due to AlN possessing a relatively higher LTC of 272 W/mK than NaH (only 14 W/mK). Regarding h-GaN/LiF in Fig. 8e, the high heat flux is more prevalent between 3 and 7 THz which is also where the phonon DOS match in Fig. 7e. The overlapped phonon states in the optical branch in h-GaN/LiF do not contribute to transporting heat flux at the interface. In h-GaN/BSb shown in Fig. 8f, the heat flux is transported by frequencies between 3 and 6 THz and the optical branch frequencies between 16 and 18 THz do not transport significant amount of heat flux even though the phonon DOS overlaps at those frequencies. It can also be noted that the maximum heat flux of 52 MW/m^2 in h-GaN/BSb is higher than the maximum heat flux of 26 MW/m^2 in h-GaN/LiF due to the higher LTC in BSb than LiF. As seen from these results, the optical phonons generally do not transport heat flux much although phonon DOS overlaps in these regions. This further demonstrates that the average $\overline{GV_1} \times \overline{GV_2}$ should only be taken in the acoustic branches in the overlap region to better explain and understand the ITC trend in Fig. 6. Fig. 8 also highlights the importance of high LTC of heat sinks or

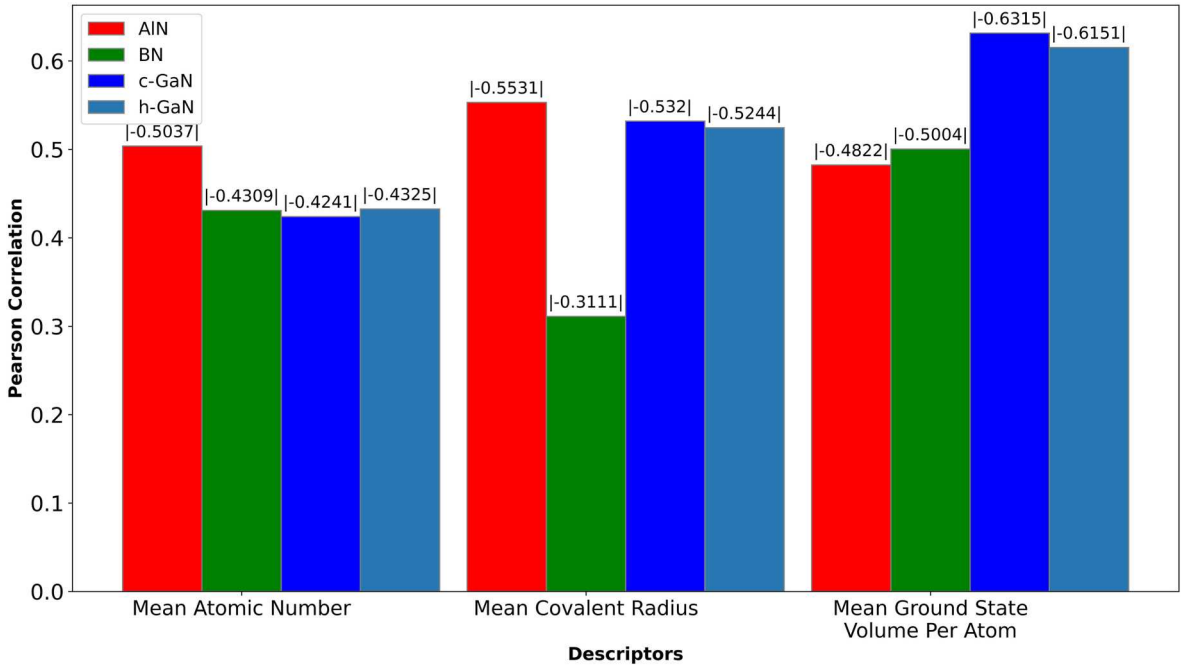

Fig. 9. Absolute Pearson correlation values of mean atomic number, mean covalent radius, and mean ground state volume per atom correlated with ITC. 900 to 1000 datapoints of ITC with AlN, BN, c-GaN, and h-GaN as heat sources are used for the analysis. The color represents different heat sources. The original negative Pearson correlation values indicate that the ITC negatively depends on all descriptors.

substrates in thermal management applications, as high LTC indicates high heat flux that can be quickly dissipated in the substrates once being transported across the interface.

d) Pearson correlation analysis of simple material descriptors for ITC

Although Fig. 6 shows a clear trend among ITC with phonon DOS overlap and our proposed group velocity descriptor, the group velocities involved in $\overline{GV_1} \times \overline{GV_2}$ are hard to calculate since it requires the calculation of second order IFC which is computationally expensive by DFT. Here we discuss the possibility of exploring some material descriptors with cheaper computational cost. The material descriptors studied in this work are the mean atomic number, mean covalent radius, and mean ground state volume per atom of the constituent elements in the chemical composition of the substrate materials. Features from the chemical composition of the materials can be compared with ITC using a statistical correlation measure such as Pearson correlation [18] defined as $\frac{\sum (x_i-\bar{x})(y_i-\bar{y})}{\sqrt{\sum (x_i-\bar{x})^2 \sum (y_i-\bar{y})^2}}$, where x_i is the data point for material descriptor and y_i is the corresponding ITC value, $\bar{x}$ and $\bar{y}$ is the mean value of the variable. The corresponding Pearson correlations using mean atomic number, mean covalent radius, and mean ground state volume per atom as descriptors are shown in Fig. 9 for 900 to 1000 datapoints of ITC with AlN, BN, c-GaN, and h-GaN as heat sources. Pearson correlation values are between -1 and $+1$. Strong correlation is reflected by the value close to either -1 or $+1$, whereas zero value corresponds to weak correlation. The negative (positive) values indicate negative (positive) correlation between the two features. In Fig. 9, all Pearson correlations are represented in absolute values to show the strength of the correlation, and the direction of the correlation can be seen from the sign of the values on top of the bars. All Pearson correlation values in Fig. 9 are between -0.4 and -0.6, which indicates strong negative correlation or dependence between ITC and the studied features, i.e., a lower mean value of the studied features leads to a higher ITC. For instance, a substrate with low mean atomic mass more likely has a higher phonon frequency leading to possibly a higher phonon DOS overlap with heat sources, which fulfills a good preliminary screening condition to likely obtain high ITC. The covalent radius is a measure of the atomic size that is a part of a covalent bond with the same atom. The covalent radius grows as the row in the periodic table goes down since the orbital size or energy levels increases. However, in the same row of the periodic table the covalent radius increases from left to right since the electrons undergo higher effective charge from the nucleus which decreases the covalent radius. Overall, low covalent radius from elements which possess low atomic numbers and masses should lead to similar phonon DOS overlap between the heat sources and heat sinks which have high chance to lead to high ITC. The ground state volume is the volume of the cell in ground state calculated by DFT. Low mean ground state volume per atom means the atoms are more densely packed and interatomic bonding should be strong, and usually such materials have low mean atomic numbers and possess low atomic radius. Thus, the substrates with low mean ground state volume per atom would have higher ITC. Generally speaking, similar species in terms of atomic numbers of heat sources and substrates are more likely to have higher phonon DOS overlap which might result in high ITC as well. Although the Pearson correlation values of studied material descriptors are not close to the bounds (-1 or $+1$), these descriptors provide new route for the first step of quickly screening potential substrates from large-scale hypothetical structures with very low computational cost and thus are very useful for future high-throughput material screening. We also need to point out that various limitations might occur. One could be the case when a similar average mass could occur between h-GaN and a heat sink, but the atomic masses of the heat sink might have large deviation (i.e., light and heavy elements constitute the primitive cell) in which case the heat sink will not have large phonon DOS overlap with h-GaN. Another limitation could be the low product of group velocity of acoustic branch phonons in the phonon DOS overlapped frequency region. Even if the phonon DOS overlap between h-GaN and a heat sink is high, the group velocity product of the acoustic phonon might be low which will result in lower ITC. The bottom line is that the average mass does not guarantee high ITC, but it is a good initial screening descriptor. Further fine screening could be completed by phonon DOS overlap and the average acoustic group velocity of constituting material pairs ($\overline{GV_1} \times \overline{GV_2}$) as proposed in this work.

4. Conclusion

To summarize, we constructed a CATGNN model and trained it on phonon DOS of 4994 crystal structures with 62 unique elements calculated by high precision DFT. The predicted phonon DOS results from our CATGNN model match the DFT calculations to a large extent, which demonstrates the capability of the model in predicting spectral-like materials properties. From computational speed point of view, training CATGNN model is several orders of magnitude computationally cheaper than the full DFT calculations. We further screened materials by phonon DOS overlap to discover new combinations of materials with ultrahigh interfacial thermal conductance for heat dissipation of HEMT devices. We elucidate the hidden relationship and strong correlation between high ITC and high average acoustic group velocity of both heat sources and heat sinks, along with the previously known descriptor of high phonon DOS overlap. We reveal a few unexpected cases where ultrahigh ITC does not necessarily occur at interfaces with large phonon DOS match, for example, BN/MgO interface with phonon DOS overlap of only 0.22 but ITC of 1044 MW/m^{2}K. This indicates that vibrational similarity or high phonon DOS overlap is not the only requirement to get high ITC, and the average acoustic group velocity is instead equally important. We demonstrate that, although the LTC of substrates does not have deterministic effect on ITC, it affects the magnitude of total heat flux that can be dissipated in the substrates after transporting across the interface, and therefore the traditional strategy of searching high LTC materials for heat dissipation is still valid. Finally, we conducted Pearson correlation analysis on ~1000 DFT ITC datapoints and identified a few simple material descriptors, namely mean atomic number, mean covalent radius, and mean ground state volume per atom, that are strongly but negatively correlated with ITC. These easy-to-calculate material features combined with the aforementioned criteria of high average acoustic group velocity and phonon DOS overlap offer a new and reliable route for designing and fast screening large-scale material pairs with high ITC at the interfaces for thermal management of wide bandgap HEMT electronics.

CRediT authorship contribution statement

Mohammed Al-Fahdi: Writing – original draft, Validation, Methodology, Investigation, Formal analysis, Data curation. **Changpeng Lin:** Writing – review & editing, Methodology, Investigation. **Chen Shen:** Software, Data curation. **Hongbin Zhang:** Writing – review & editing, Software, Resources, Investigation. **Ming Hu:** Writing – review & editing, Visualization, Validation, Supervision, Resources, Project administration, Investigation, Funding acquisition, Formal analysis, Conceptualization.

Declaration of Competing Interest

The authors declare that they have no known competing financial interests or personal relationships that could have appeared to influence the work reported in this paper.

Acknowledgements

This work was supported by the NSF (award number 2030128, 2110033, 2311202, 2320292), SC EPSCoR/IDeA Program under NSF OIA-1655740 (23-GC01) and ASPIRE grant from the Office of the Vice President for Research at the University of South Carolina (project 80005046). M.A. acknowledges the financial support of the SPARC Graduate Research Grant (project 80004800). C.L. acknowledges the support from the Sinergia project of the Swiss National Science Foundation (grant number CRSII5_189924).

Appendix A. Supplementary data

Supplementary data to this article can be found online at https://doi.org/10.1016/j.mtphys.2024.101632.

Data availability

The code and data are shared on the GitHub repository https://github.com/Mofahdi/CATGNN_phonon_DOS to reproduce this work. The DFT raw data for GNN model phonon DOS training and testing are provided in the Excel file "SI_DFT_data_for_CATGNN_training.xlsx" and "SI_test_dataset_for_CATGNN_model.xlsx". All DFT raw data used for obtaining hidden structure-material property relationship and performing Pearson correlation analysis for the 4 heat source materials are provided in the Excel file "SI_ITC_pdos_LTC_GV_ITC_acoustic.xlsx", where the OQMD ID of the two materials forming the interface, LTC along three directions, phonon DOS overlap, average acoustic group velocity, and corresponding ITC calculated by almaBTE are given. Other data are available from the corresponding author upon reasonable request.

References

[1] J. Schmidt, M.R. Marques, S. Botti, M.A. Marques, Recent advances and applications of machine learning in solid-state materials science, npj Comput. Mater. 5 (1) (2019) 83.
[2] P. Schlexer Lamoureux, K.T. Winther, J.A. Garrido Torres, V. Streibel, M. Zhao, M. Bajdich, F. Abild-Pedersen, T. Bligaard, Machine learning for computational heterogeneous catalysis, ChemCatChem 11 (16) (2019) 3581–3601.
[3] C. Chen, Y. Zuo, W. Ye, X. Li, Z. Deng, S.P. Ong, A critical review of machine learning of energy materials, Adv. Energy Mater. 10 (8) (2020): 1903242.
[4] M. Al-Fahdi, M. Hu, High throughput substrate screening for interfacial thermal management of β-Ga2o3 by deep convolutional neural network, J. Appl. Phys. 135 (20) (2024): 205101.
[5] M. Al-Fahdi, K. Yuan, Y. Yao, R. Rurali, M. Hu, High-throughput thermoelectric materials screening by deep convolutional neural network with fused orbital field matrix and composition descriptors, Appl. Phys. Rev. 11 (2) (2024): 021402.
[6] Y. Zhao, E.M. Siriwardane, Z. Wu, N. Fu, M. Al-Fahdi, M. Hu, J. Hu, Physics guided deep learning for generative design of crystal materials with symmetry constraints, npj Comp. Mater. 9 (1) (2023) 38.
[7] Y. Zhao, M. Al-Fahdi, M. Hu, E.M. Siriwardane, Y. Song, A. Nasiri, J. Hu, High-throughput discovery of novel cubic crystal materials using deep generative neural networks, Adv. Sci. 8 (20) (2021): 2100566.
[8] J.E. Saal, S. Kirklin, M. Aykol, B. Meredig, C. Wolverton, Materials design and discovery with high-throughput density functional theory: the open Quantum materials database (OQMD), JOM 65 (11) (2013) 1501–1509.
[9] K. Choudhary, K.F. Garrity, A.C. Reid, B. DeCost, A.J. Biacchi, A.R. Hight Walker, Z. Trautt, J. Hattrick-Simpers, A.G. Kusne, A. Centrone, A. Davydov, J. Jiang, R. Pachter, G. Cheon, E. Reed, A. Agrawal, X. Qian, V. Sharma, H. Zhuang, S. V. Kalinin, B.G. Sumpter, G. Pilania, P. Acar, S. Mandal, K. Haule, D. Vanderbilt, K. Rabe, F. Tavazza, The joint automated repository for various integrated simulations (jarvis) for data-driven materials design, npj Comput. Mater. 6 (1) (2020) 173.
[10] S. Curtarolo, W. Setyawan, S. Wang, J. Xue, K. Yang, R.H. Taylor, L.J. Nelson, G.L. W. Hart, S. Sanvito, Buongiorno-Nardelli, M.; Mingo, N.; Levy, O. AFLOWLIB. ORG: A Distributed Materials Properties Repository from High-Throughput Ab Initio Calculations, Comput. Mater. Sci. 58 (2012) 227–235.
[11] C. Draxl, M. Scheffler, The NOMAD laboratory: from data sharing to artificial intelligence, J. Phys. Mater. 2 (3) (2019): 036001.
[12] L. Chanussot, A. Das, S. Goyal, T. Lavril, M. Shuaibi, M. Riviere, K. Tran, J. Heras-Domingo, C. Ho, W. Hu, A. Palizhati, A. Sriram, B. Wood, J. Yoon, D. Parikh, C. L. Zitnick, Z. Ulissi, Open catalyst 2020 (OC20) dataset and community challenges, ACS Catal. 11 (10) (2021) 6059–6072.
[13] A. Jain, S.P. Ong, G. Hautier, W. Chen, W.D. Richards, S. Dacek, S. Cholia, D. Gunter, D. Skinner, G. Ceder, K.A. Persson, Commentary: the materials project: a materials genome approach to accelerating materials innovation, Apl. Mater. 1 (1) (2013): 011002.
[14] N.R. Scott, D.L. Stoddard, M.D. Nelms, Z. Wallace, I. Turner, L. Turner, M. Croom, K. Franklin, S. Sandifer, M.S. Ali Al-fahdi, T. Butler, A.M. Rajendran, Experimental and computational characterization of glass microsphere-cementitious composites, Cement Concr. Res. 152 (2022): 106671.
[15] A. Wang, R. Murdock, S. Kauwe, A. Oliynyk, A. Gurlo, J. Brgoch, K. Persson, T. Sparks, Machine Learning for Materials Scientists: an Introductory Guide towards Best Practices, 2020.
[16] K. Choudhary, B. DeCost, F. Tavazza, Machine learning with force-field-inspired descriptors for materials: fast screening and mapping energy landscape, Phys. Rev. Mater. 2 (8) (2018): 083801.

[17] J.P. Lightstone, L. Chen, C. Kim, R. Batra, R. Ramprasad, Refractive index prediction models for polymers using machine learning, J. Appl. Phys. 127 (21) (2020): 215105.

[18] Y. Zhuo, A. Mansouri Tehrani, J. Brgoch, Predicting the band gaps of inorganic solids by machine learning, J. Phys. Chem. Lett. 9 (7) (2018) 1668–1673.

[19] S.R. Xie, Y. Quan, A.C. Hire, B. Deng, J.M. DeStefano, I. Salinas, U.S. Shah, L. Fanfarillo, J. Lim, J. Kim, G.R. Stewart, J.J. Hamlin, P.J. Hirschfeld, R. G. Hennig, Machine learning of superconducting critical temperature from eliashberg theory, npj Comput. Mater. 8 (1) (2022) 14.

[20] J. Ojih, A. Rodriguez, J. Hu, M. Hu, Screening outstanding mechanical properties and low lattice thermal conductivity using global attention graph neural network, Energy and AI 14 (2023) 100286.

[21] M. Al-Fahdi, T. Ouyang, M. Hu, High-throughput computation of novel ternary B–C–N structures and carbon allotropes with electronic-level insights into superhard materials from machine learning, J. Mater. Chem. A 9 (48) (2021) 27596–27614.

[22] J. Ojih, M. Al-Fahdi, A.D. Rodriguez, K. Choudhary, M. Hu, Efficiently searching extreme mechanical properties via boundless objective-free exploration and minimal first-principles calculations, npj Comput. Mater. 8 (1) (2022).

[23] M. Al-Fahdi, A. Rodriguez, T. Ouyang, M. Hu, High-throughput computation of new carbon allotropes with diverse hybridization and ultrahigh hardness, Crystals 11 (7) (2021) 783.

[24] Y. Ouyang, Z. Zhang, C. Yu, J. He, G. Yan, J. Chen, Accuracy of machine learning potential for predictions of multiple-target physical properties, Chin. Phys. Lett. 37 (12) (2020): 126301.

[25] Y. Xu, G. Wang, Y. Zhou, Broadly manipulating the interfacial thermal energy transport across the Si/4H-SiC interfaces via nanopatterns, Int. J. Heat Mass Transf. 187 (2022): 122499.

[26] Y. Ouyang, C. Yu, J. He, P. Jiang, W. Ren, J. Chen, Accurate description of high-order phonon anharmonicity and lattice thermal conductivity from molecular dynamics simulations with machine learning potential, Phys. Rev. B 105 (11) (2022): 115202.

[27] J. Ojih, M. Al-Fahdi, Y. Yao, J. Hu, M. Hu, Graph theory and graph neural network assisted high-throughput crystal structure prediction and screening for energy conversion and storage, J. Mater. Chem. A 12 (14) (2024) 8502–8515.

[28] T. Zhu, R. He, S. Gong, T. Xie, P. Gorai, K. Nielsch, J.C. Grossman, Charting lattice thermal conductivity for inorganic crystals and discovering rare earth chalcogenides for thermoelectrics, Energy Environ. Sci. 14 (6) (2021) 3559–3566.

[29] A. Rodriguez, C. Lin, C. Shen, K. Yuan, M. Al-Fahdi, X. Zhang, H. Zhang, M. Hu, Unlocking phonon properties of a large and diverse set of cubic crystals by indirect bottom-up machine learning approach, Commun. Mater. 4 (1) (2023) 61.

[30] A. Rodriguez, C. Lin, H. Yang, M. Al-Fahdi, C. Shen, K. Choudhary, Y. Zhao, J. Hu, B. Cao, H. Zhang, M. Hu, Million-scale data integrated deep neural network for phonon properties of heuslers spanning the periodic table, npj Comp. Mater. 9 (1) (2023).

[31] Z. Chen, N. Andrejevic, T. Smidt, Z. Ding, Q. Xu, Y.T. Chi, Q.T. Nguyen, A. Alatas, J. Kong, M. Li, Direct prediction of phonon density of states with euclidean neural networks, Adv. Sci. 8 (12) (2021): 2004214.

[32] R.M. Martin, Electronic Structure: Basic Theory and Practical Methods, Cambridge University Press, Cambridge etc, 2020.

[33] B.G. del Rio, C. Kuenneth, H.D. Tran, R. Ramprasad, An efficient deep learning scheme to predict the electronic structure of materials and molecules: the example of graphene-derived allotropes, J. Phys. Chem. A 124 (45) (2020) 9496–9502.

[34] C. Ben Mahmoud, A. Anelli, G. Csányi, M. Ceriotti, Learning the electronic density of states in condensed matter, Phys. Rev. B 102 (23) (2020): 235130.

[35] Z. Wu, S. Pan, F. Chen, G. Long, C. Zhang, P.S. Yu, A comprehensive survey on graph neural networks, IEEE Trans. Neural Net. Lear. 32 (1) (2021) 4–24.

[36] V.P. Dwivedi, C.K. Joshi, T. Laurent, Y. Bengio, X. Bresson, Benchmarking graph neural networks, arXiv (2003): 00982. Preprint at, https://arxiv.org/abs/2003.00982.

[37] Z. Guo, H. Wang, A deep graph neural network-based mechanism for social recommendations, IEEE Trans. Industr. Inform. 17 (4) (2021) 2776–2783.

[38] M.T.D. Parise, D. Parise, R.B. Kato, J.K. Pauling, A. Tauch, V.A. de Carvalho Azevedo, J. Baumbach, CoryneRegNet 7, the reference database and analysis platform for corynebacterial gene regulatory networks, Sci. Data 7 (2020) 142.

[39] X. Li, Y. Zhou, N. Dvornek, M. Zhang, S. Gao, J. Zhuang, D. Scheinost, L.H. Staib, P. Ventola, J.S. Duncan, Braingnn: interpretable brain graph neural network for fmri analysis, Med. Image Anal. 74 (2021): 102233.

[40] K. Choudhary, B. DeCost, Atomistic line graph neural network for improved materials property predictions, npj Comput. Mater. 7 (1) (2021) 185.

[41] F. Scarselli, M. Gori, Chung Tsoi Ah, M. Hagenbuchner, G. Monfardini, The graph neural network model, IEEE Trans. Neural Netw. 20 (1) (2009) 61–80.

[42] T. Xie, J.C. Grossman, Crystal graph convolutional neural networks for an accurate and interpretable prediction of material properties, Phys. Rev. Lett. 120 (14) (2018).

[43] S.-Y. Louis, Y. Zhao, A. Nasiri, X. Wang, Y. Song, F. Liu, J. Hu, Graph convolutional neural networks with global attention for improved materials property prediction, Phys. Chem. Chem. Phys. 22 (32) (2020) 18141–18148.

[44] V. Fung, J. Zhang, E. Juarez, B.G. Sumpter, Benchmarking graph neural networks for materials chemistry, npj Comput. Mater. 7 (1) (2021) 84.

[45] Z. Cheng, F. Mu, L. Yates, T. Suga, S. Graham, Interfacial thermal conductance across room-temperature-bonded Gan/diamond interfaces for Gan-on-Diamond devices, ACS Appl. Mater. Interfaces 12 (7) (2020) 8376–8384.

[46] H. Guo, Y. Kong, T. Chen, Thermal simulation of high power Gan-on-Diamond substrates for HEMT applications, Diam. Relat. Mater. 73 (2017) 260–266.

[47] G. Kresse, J. Furthmüller, Efficiency of AB-initio total energy calculations for metals and semiconductors using a plane-wave basis set, Comput. Mater. Sci. 6 (1) (1996) 15–50.

[48] G. Kresse, J. Furthmüller, Efficient iterative schemes for *Ab Initio* total-energy calculations using a plane-wave basis set, Phys. Rev. B 54 (16) (1996) 11169–11186.

[49] G. Kresse, D. Joubert, From ultrasoft pseudopotentials to the projector augmented-wave method, Phys. Rev. B 59 (3) (1999) 1758–1775.

[50] J.P. Perdew, K. Burke, M. Ernzerhof, Generalized gradient approximation made simple, Phys. Rev. Lett. 77 (18) (1996) 3865–3868.

[51] P.E. Blöchl, Projector augmented-wave method, Phys. Rev. B 50 (24) (1994) 17953–17979.

[52] H.J. Monkhorst, J.D. Pack, Special points for brillouin-zone integrations, Phys. Rev. B 13 (12) (1976) 5188–5192.

[53] Fei Zhou, Weston Nielson, Yi Xia, Vidvuds Ozoliņš, Lattice anharmonicity and thermal conductivity from compressive sensing of first-principles calculations, Phys. Rev. Lett. 113 (2014): 185501.

[54] Fei Zhou, Weston Nielson, Yi Xia, Vidvuds Ozoliņš, Compressive sensing lattice dynamics. I. General formalism, Phys. Rev. B 100 (2019): 184308.

[55] Fei Zhou, Babak Sadigh, Daniel Åberg, Yi Xia, Vidvuds Ozoliņš, Compressive sensing lattice dynamics. II. Efficient phonon calculations and long-range interactions, Phys. Rev. B 100 (2019): 184309.

[56] A. Togo, I. Tanaka, First principles phonon calculations in materials science, Scr. Mater. 108 (2015) 1–5.

[57] W. Li, J. Carrete, A. Katcho, N. Mingo, N. Shengbte, A solver of the Boltzmann transport equation for phonons, Comput. Phys. Commun. 185 (6) (2014) 1747–1758.

[58] J. Carrete, B. Vermeersch, A. Katre, A. van Roekeghem, T. Wang, G.K.H. Madsen, N. Almabte Mingo, A solver of the space–time dependent Boltzmann transport equation for phonons in structured materials, Comput. Phys. Commun. 220 (2017) 351–362.

[59] S.-Y. Yue, T. Xu, B. Liao, Ultralow thermal conductivity in a two-dimensional material due to surface-enhanced resonant bonding, Materials Today Physics 7 (2018) 89–95.

[60] M. Al-Fahdi, X. Zhang, M. Hu, Phonon transport anomaly in metavalent bonded materials: contradictory to the conventional theory, J. Mater. Sci. 56 (33) (2021) 18534–18549.

[61] J. Liu, Y. Zhao, Z. Dai, J. Ni, S. Meng, Low thermal conductivity and good thermoelectric performance in mercury chalcogenides, Comput. Mater. Sci. 188 (2021): 110192.

[62] H. Peng, N. Kioussis, D.A. Stewart, Anisotropic lattice thermal conductivity in chiral tellurium from first principles, Appl. Phys. Lett. 107 (25) (2015).

[63] K. Yuan, X. Zhang, D. Tang, M. Hu, Anomalous pressure effect on the thermal conductivity of zno, Gan, and AlN from first-principles calculations, Phys. Rev. B 98 (14) (2018).

[64] H. Wang, G. Qin, Z. Qin, G. Li, Q. Wang, M. Hu, Lone-pair electrons do not necessarily lead to low lattice thermal conductivity: an exception of two-dimensional penta-CN2, J. Phys. Chem. Lett. 9 (10) (2018) 2474–2483.

[65] G. Qin, A. Huang, Y. Liu, H. Wang, Z. Qin, X. Jiang, J. Zhao, J. Hu, M. Hu, High-throughput computational evaluation of lattice thermal conductivity using an optimized Slack model, Materials Advances 3 (17) (2022) 6826–6830.

[66] Z. Chang, K. Yuan, J. Li, Z. Sun, Jiongzhi Zheng, Mohammed Al-Fahdi, Yufei Gao, Wei Bin, Xiaoliang Zhang, Ming Hu, Dawei Tang, Anomalous thermal conductivity induced by high dispersive optical phonons in rubidium and cesium halides, ESEE 16 (2022) 30–39.

[67] N. Ketkar, J. Moolayil, Automatic differentiation in deep learning, Deep Learning with Python (2021) 133–145.

[68] Matthias Fey, Jan E. Lenssen, Fast graph representation learning with PyTorch geometric, Preprint at (2019). https://arxiv.org/abs/1903.02428.

[69] M. Geiger, T. Smidt, e3nn: Euclidean neural networks, arXiv preprint arXiv: 2207.09453 (2022).

[70] N. Thomas, T. Smidt, S. Kearnes, L. Yang, L. Li, K. Kohlhoff, P. Riley, Tensor field networks: rotation-and translation-equivariant neural networks for 3d point clouds, arXiv preprint arXiv:1802.08219 (2018).

[71] Q. Wang, X. Wang, X. Liu, J. Zhang, Interfacial engineering for the enhancement of interfacial thermal conductance in Gan/aln heterostructure, J. Appl. Phys. 129 (23) (2021): 235102.

[72] A.L. Moore, L. Shi, Emerging challenges and materials for thermal management of electronics, Mater. Today 17 (4) (2014) 163–174.

[73] Z. Chang, J. Ma, K. Yuan, J. Zheng, B. Wei, M. Al-Fahdi, Y. Gao, X. Zhang, H. Shao, M. Hu, D. Tang, Zintl phase compounds Mg3Sb2−XBix (x = 0, 1, and 2) monolayers: electronic, phonon and thermoelectric properties from Ab Initio calculations, Front. Mech. Eng. 8 (2022).

[74] S. Mizuno, Y. Ohno, S. Kishimoto, K. Maezawa, T. Mizutani, Large gate leakage current in algan/Gan high electron mobility transistors, Jpn. J. Appl. Phys. 41 (8) (2002) 5125–5126.

[75] Z. Yatabe, J.T. Asubar, T. Hashizume, Insulated gate and surface passivation structures for GAN-based power transistors, J. Phys. D Appl. Phys. 49 (39) (2016): 393001.

[76] M. Whiteside, S. Arulkumaran, G.I. Ng, Demonstration of vertically-ordered h-bn/algan/Gan metal-insulator-semiconductor high-electron-mobility transistors on Si substrate, Mater. Sci. Eng. B 270 (2021): 115224.

[77] S. Liu, W. Zhang, J. Zhang, X. Song, Y. Wu, D. Chen, S. Xu, S. Zhao, Y. Hao, ALN/Gan superlattice channel hemts on silicon substrate, IEEE T. Electron Dev. 68 (7) (2021) 3296–3301.

[78] F.Z. Bechlaghem, A. Hamdoune, 3D Simulation and Optimization of Characteristics of al0.1ga0.9n/in0.2ga0.8n High Electron Mobility Transistor with b0.03ga0.97n Back-Barrier Layer, 2021.
[79] M. Abe, Cubic Gan/algan hemts on 3c-sic substrate for normally-off operation, IEICE Trans. Electron. E89-C (7) (2006) 1057–1063.
[80] R. Granzner, E. Tschumak, M. Kittler, K. Tonisch, W. Jatal, J. Pezoldt, D. As, F. Schwierz, Vertical design of cubic Gan-based high electron mobility transistors, J. Appl. Phys. 110 (11) (2011): 114501.
[81] A. Ward, D.A. Broido, D.A. Stewart, G. Deinzer, *Ab Initio*Theory of the lattice thermal conductivity in diamond, Phys. Rev. B 80 (12) (2009): 125203.
[82] K. Yuan, X. Zhang, D. Tang, M. Hu, Anomalous pressure effect on the thermal conductivity of zno, Gan, and AlN from first-principles calculations, Phys. Rev. B 98 (14) (2018).
[83] W.A. Little, The transport of heat between dissimilar solids at low temperatures, Can. J. Phys. 37 (3) (1959) 334–349.
[84] Y. Zhang, D. Ma, Y. Zang, X. Wang, N. Yang, A modified theoretical model to accurately account for interfacial roughness in predicting the interfacial thermal conductance, Front. Energy Res. 6 (2018).
[85] A.N. Smith, P.M. Norris, J.L. Hostetler, Thermal boundary resistance measurements using a transient thermoreflectance technique. Microscale thermophys, Eng. 4 (1) (2000) 51–60.
[86] Y. Liu, Z.-Y. Ong, J. Wu, Y. Zhao, K. Watanabe, T. Taniguchi, D. Chi, G. Zhang, J. T. Thong, C.-W. Qiu, K. Hippalgaonkar, Thermal conductance of the 2d mos2/h-BN and graphene/h-BN interfaces, Sci. Rep. 7 (1) (2017).
[87] Y. Zhou, X. Zhang, M. Hu, Quantitatively analyzing phonon spectral contribution of thermal conductivity based on nonequilibrium molecular dynamics simulations. I. From space fourier transform, Phys. Rev. B 92 (19) (2015): 195204.
[88] Y. Zhou, M. Hu, Quantitatively analyzing phonon spectral contribution of thermal conductivity based on nonequilibrium molecular dynamics simulations. II. From time fourier transform, Phys. Rev. B 92 (19) (2015): 195205.
[89] J. Dai, Z. Tian, Rigorous formalism of anharmonic atomistic green's function for three-dimensional interfaces, Phys. Rev. B 101 (4) (2020): 041301 (R).
[90] J.-S. Wang, J. Wang, N. Zeng, Nonequilibrium Green's function approach to mesoscopic thermal transport, Phys. Rev. B 74 (3) (2006): 033408.
[91] P. Reddy, K. Castelino, A. Majumdar, Diffuse mismatch model of thermal boundary conductance using exact phonon dispersion, Appl. Phys. Lett. 87 (21) (2005): 211908.
[92] D.B. Brown, T.L. Bougher, X. Zhang, P.M. Ajayan, B.A. Cola, S. Kumar, Thermal boundary conductance and phonon transmission in hexagonal boron nitride/graphene heterostructures, physica status solidi (a) 216 (23) (2019): 1900446.
[93] X. Huang, Z. Guo, Thermal effect of epilayer on phonon transport of semiconducting heterostructure interfaces, Int. J. Heat Mass Transf. 178 (2021): 121613.
[94] X. Huang, Z. Guo, High thermal conductance across c-BN/diamond interface, Diam. Relat. Mater. 108 (2020): 107979.
[95] H. Zhou, Z.-Y. Ong, G. Zhang, Y.-W. Zhang, Computational predictions of Quantum thermal transport across nanoscale interfaces, Nanoscale 14 (2022) 9209–9217.
[96] Z. Sun, K. Yuan, X. Zhang, D. Tang, First-principles calculations of interfacial thermal transport properties between SIC/Si substrates and compounds of boron with selected group V elements, Phys. Chem. Chem. Phys. 21 (11) (2019) 6011–6020.
[97] W. Bao, Z. Wang, D. Tang, Phonon transport across Gan/ALN interface: interfacial phonon modes and phonon local non-equilibrium analysis, Int. J. Heat Mass Transf. 183 (2022): 122090.
[98] A. Spindlberger, D. Kysylychyn, L. Thumfart, R. Adhikari, A. Rastelli, A. Bonanni, Cross-plane thermal conductivity of Gan/ALN superlattices, Appl. Phys. Lett. 118 (6) (2021): 062105.
[99] J.S. Kang, M. Li, H. Wu, H. Nguyen, T. Aoki, Y. Hu, Integration of boron arsenide cooling substrates into gallium nitride devices, Nat. Electron. 4 (6) (2021) 416–423.
[100] S. Khan, F. Angeles, J. Wright, S. Vishwakarma, V.H. Ortiz, E. Guzman, F. Kargar, A.A. Balandin, D.J. Smith, D. Jena, H.G. Xing, R. Wilson, Properties for thermally conductive interfaces with wide band gap materials, ACS Appl. Mater. Interfaces 14 (31) (2022) 36178–36188.